THESIS

# DATA-DRIVEN MODELS FOR SUBSEASONAL CYCLOGENESIS FORECASTS IN THE EAST PACIFIC AND NORTH ATLANTIC

Submitted by
Zaibeth Carlo Frontera
Department of Atmospheric Science

In partial fulfillment of the requirements
For the Degree of Master of Science
Colorado State University
Fort Collins, Colorado
Summer 2024

Master's Committee:

Advisor: Elizabeth A. Barnes
Co-Advisor: Eric Maloney

G. Brooke Anderson

# ABSTRACT

## DATA-DRIVEN MODELS FOR SUBSEASONAL CYCLOGENESIS FORECASTS IN THE EAST PACIFIC AND NORTH ATLANTIC

Tropical cyclones (TCs) are hazardous and financially burdensome meteorological events. Previous studies have revealed that longer timescale phenomena, including the El Niño Southern Oscillation (ENSO), the Madden-Julian Oscillation (MJO), and African Easterly Waves, influence TC development by modifying large-scale environmental conditions such as vertical wind shear, mid-level moisture, and sea surface temperatures. Statistical models have been developed to forecast TCs in the Atlantic and Pacific basins by incorporating information about ENSO and the MJO. Expanding on this work, we employ logistic regression (LR) and neural network (NN) models with an extended set of variables to predict cyclogenesis on subseasonal timescales for the east Pacific and Atlantic regions. These models utilize ENSO and MJO indices, along with other local environmental information, and demonstrate enhanced forecasting skill relative to models that only use TC climatology. Overall, the NN model shows superior performance compared to the LR model, retaining skill out to three weeks leadtime for the east Pacific, and out to four weeks for the Atlantic basin. The predictive capabilities of the model are demonstrated for the years 1983 and 2021. To gain insights into the decision-making process of the NN models, an AI explainability technique is employed to understand which features are considered important in making the predictions. For both basins, the addition of ENSO and MJO information prove to be essential for the superior forecast skill of the NN model.

# TABLE OF CONTENTS

# Chapter 1

# Introduction

Since 1980, the United States has allocated over 1 billion dollars to address the impacts from at least 355 weather and climate events, with 60 of them being tropical cyclones (TCs) that caused damage exceeding 1.3 trillion dollars. Although TCs constitute only one-fifth of these 355 events, they account for more than half (53%) of the billion-dollar weather and climate disasters (NOAA NCEI 2023). Therefore, it is crucial to ensure accurate and reliable TC forecasts. Phenomena such as El Niño Southern Oscillation (ENSO) and the Madden-Julian Oscillation (MJO) influence TC activity by affecting large-scale environmental factors like vertical wind shear, mid-level moisture, sea level pressure, and sea surface temperatures (SSTs) (Reed et al.1977; Gray 1984; Goldenberg and Shapiro 1996; Fink and Reiner 2003; Kiladis et al. 2006; Camargo et al. 2009; Klotzbach 2014, and references therein).

The MJO is a significant mode of tropical variability characterized by a period of 30-60 days. Originating in the Indo-Pacific Ocean, the MJO dominates the variability in the tropical atmosphere on subseasonal timescales (Madden and Julian 1971, 1972). Wheeler and Hendon (2004) described the MJO by phases, or position along the equator as convection moves eastward. Phase 1 has enhanced convection over the western Indian Ocean, and the final phase before the cycle begins again is phase 8, when convection reaches the central Pacific. In the eastern Pacific, Maloney and Hartmann (2000) found that the number of hurricanes is over four times higher during MJO phase 2 compared to phase 6. This hurricane modulation is initiated by 850-mb MJO zonal wind anomalies that propagate from the west to east Pacific (Maloney and Hartmann 2000). These zonal wind anomalies can either enhance or suppress convection in the east Pacific, with westerlies intensifying convection and easterlies weakening it. When periods of westerly 850-mb equatorial zonal wind anomalies occur over the east Pacific, they create conditions optimal for the formation and development of TCs (Maloney and Hartmann 2000). In the Atlantic, it has been shown that the MJO plays a role in the clustering of Atlantic TCs (Maloney and Hartmann 2000b; Maloney and Shaman 2008; Klotzbach and Oliver 2015). For instance, when the zonal wind anomalies associated with the MJO are westerly at low levels, the Gulf of Mexico and the West Caribbean experience a four-fold increase in the probability of cyclogenesis (Maloney and Hartmann 2000b). Phases 1-3 of the MJO are associated with an active Atlantic basin, while phases 5-7 are typically linked to calm periods (Klotzbach and Oliver 2015). These connections between the MJO and TC activity in the east Pacific and the Atlantic highlight the usefulness of MJO information in a TC genesis forecasting model.

Clear relationships also exist between ENSO and cyclogenesis (Gray 1984; Goldenberg and Shapiro 1996). In the east Pacific, the number of observed TCs is twice as high during El Niño compared to La Niña. During La Niña, negative SST anomalies are observed over the east Pacific. These conditions suppress hurricane development in the east Pacific (Kim et al. 2011). Conversely, El Niño is associated with warm anomalies over the east Pacific and a decrease in vertical shear over the central Pacific, which favor TC formation in both regions (Kim et al. 2011). ENSO also impacts the Atlantic Ocean through changes in the Walker circulation. During El Niño, the Walker circulation weakens significantly and shifts eastward, leading to increased westerlies at higher levels over the tropical Atlantic. These strong westerlies, combined with weak easterlies at lower levels, create strong wind shear over the region (e.g. Shaman et al. 2009). Since strong wind shear hinders cyclogenesis, less TC activity in the Atlantic is observed during El Niño periods.

Conversely, during La Niña, convection intensifies and wind shear decreases over the western Atlantic facilitating TC formation (Gray 1984; Goldenberg and Shapiro 1996).

African easterly wave (AEW) activity may also serve as a good a cyclogenesis predictor. AEWs are synoptic disturbances that traverse from west Africa into the Atlantic, typically with a period of two to five days (Adames 2021). These waves develop near the African easterly jet. The vorticity from the AEW combines with locally generated vorticity from convection, create favorable conditions for cyclogenesis (Hopsch et al. 2010). Additionally, Dieng et al. (2017) proposed that TC genesis is influenced by sustained convection over the ocean within the troughs. AEWs are considered the primary precursors to Atlantic hurricanes, with approximately 60% of TCs originating from AEWs (Landsea 1993). Moreover, Thorncroft and Hodges (2001) found positive correlations between AEW activity and Atlantic TC activity over a period of 45 years, supporting the use of AEWs as a TC genesis predictor.

The relationship between SSTs and TCs has been studied for decades, with early studies suggesting the SST threshold needed for TC formation to be $26° - 27°$ C (Palmén 1949). Low SSTs can limit the local energy source and, consequently, cyclogenesis (Bister and Emanuel 1998). This is because the SST has a strong influence on surface fluxes and boundary layer humidity (Anthes 1982; Emanuel 1994). Hence, SST anomalies in the east Pacific and in the Atlantic Main Development Region (MDR; $5° - 18°$ N, $20° - 60°$ W) have a significant connection to TC activity. Warm anomalies in the MDR are associated with an increase in TC activity (Emanuel and Mann 2006, Elsner 2006). Moreover, the MDR SSTs can also serve as a proxy for the Atlantic Meridional Oscillation (AMO), particularly when considering the MDR SSTs relative to the tropical average SSTs (Emanuel 2005; Bell and Chelliah 2006; Vecchi et al. 2008).The AMO has been found to affect hurricane counts with a timescale of 60 - 80 years (Schlesinger and Ramankutty 1994). MDR

SSTs are often used instead of an AMO index because statistical inconsistencies exist between the AMO indices (Goldenberg et al. 2001).

Previous data-driven statistical models such as those of Gray (1984b), Saunders and Lea (2005), Leroy and Wheeler (2008), and Henderson and Maloney (2013) have made TC genesis forecasts for different ocean basins using climates variables as predictors, e.g. MJO and ENSO indices. Leroy and Wheeler (2008) employed a logistic regression model that used five predictors to predict the probability of TC genesis in the Southern Hemisphere. The five chosen predictors included a climatological seasonal cycle of TC activity, two indices representing MJO propagation, and two representing the leading patterns of interannual SST variability in the Indo-Pacific Oceans. With a logistic regression model and these predictors, Leroy and Wheeler (2008) obtained increased skill out to approximately three weeks relative to climatology. Based on Leroy and Wheeler (2008), Henderson and Maloney (2013) developed a statistical model via logistic regression for the east Pacific and the Atlantic. Their predictors included a climatology of TC genesis, an ENSO index, and two MJO indices. For the Atlantic, they included an additional predictor to represent the MDR's SST variability. Henderson and Maloney (2013) obtained skill out to three weeks relative to climatology in the east Pacific, and out to two weeks in the Atlantic.

Henderson and Maloney (2013) successfully built a logistic regression model and made forecasts using ENSO, MJO, and MDR SSTs, and we improve upon these results by including additional environmental information, increasing the statistical model's complexity, and adding 8 more years of data. In this work, data-driven models are developed using data from past tropical storms (TS) occurrence as a function of time of year in the east Pacific and the north Atlantic, along with ENSO, MJO, and daily local winds and SSTs to forecast TS genesis within a given week. While previous research has predominantly relied on climate-related data, relatively few studies have placed a significant emphasis on the integration of environmental data to study TS cyclogenesis on subseasonal timescales. These environmental variables harbor essential information that directly pertains to the assessment of cyclogenesis probabilities within a specific region. Two models, a logistic regression and a neural network, are constructed for each basin (east Pacific and Atlantic basin) and Atlantic subregions. Neural networks are employed to enhance the modeling sophistication in comparison to conventional forecasting techniques, notably logistic regression. Neural networks are characterized by their multilayer architecture, which stands in contrast to the zero-layer structure of logistic regression models. Consequently, neural networks exhibit greater architectural complexity and allow for further nonlinearity. For the NN and LR models, the Brier skill score is computed for a range of subseasonal leadtimes and several variable combinations to determine which model performs best. The goal is to make subseasonal forecasts of systems achieving 34 knot strength, which we define as a threshold for cyclogenesis (e.g., Henderson and Maloney 2013).

# Chapter 2

# Methods

## 2.1 Data Collection

This study focuses on two regions, namely the east Pacific ($5° - 25°$ N, $120° - 90°$ W) and the north Atlantic basin ($5° - 45°$ N, $100° - 15°$ W) from 1979 to 2021. To develop the data-driven models, a set of meteorological and climatological variables previously shown to impact cyclogenesis are considered as predictors. In the east Pacific region, the selected features for model input include the historical count of storms that underwent cyclogenesis within the region (referred to as TS count) as a function of calendar day, an ENSO index, two time series that characterize MJO activity, and local zonal winds and SST. For the Atlantic region, TS counts, and ENSO, MJO, AEW, and MDR SST indices are used. Throughout this study the TS counts by calendar day serve as the cyclogenesis climatology for each region.

Tropical cyclone information is obtained from the National Hurricane Center's (NHC) HURDAT2 (HURricane DATabase $2^{nd}$ generation) (Landsea and Franklin 2015). HURDAT provides comprehensive and official assessments from the NHC for storms occurring in the Atlantic and Pacific basins. The HURDAT dataset includes information such as date and time, intensity, wind radii, and location every six hours for all systems that attain tropical depression strength (less than 33 knots).

The ENSO index utilized in this study is the Niño3.4 index, developed by the National Oceanic and Atmospheric Administration (NOAA) (Rayner et. al. 2003). This index includes monthly values dating back to 1870 and employs a 5-month running mean of the SST anomalies within the region between $5^{\circ}$ N - $5^{\circ}$ S, $170^{\circ} - 120^{\circ}$ W.

MJO information is incorporated into the statistical models as the first two principal components, RMM1 and RMM2, as defined by a combined empirical orthogonal analysis that isolates MJO variability (Wheeler and Hendon 2004). RMM1 and RMM2 characterize the evolution and intensity of the MJO along the equator. In the case of the east Pacific, the RMM1 and RMM2 were also lagged by seven days (RMM1-7, RMM2-7) from the day of forecast and included as additional predictors.

The meteorological variables used as model input, specifically daily SSTs and winds from 1979 to 2021, were obtained through the ERA5 Reanalysis Data from the European Centre for Medium-Range Weather Forecasts (ECMWF) (Hersbach, H. et al., 2018; Muñoz Sabater, J., 2019). The ERA5 dataset provides hourly gridded data for atmospheric and ocean variables. Using the SST and winds over each region (Fig.1), zonal wind and SST indices are created for the east Pacific, and MDR SST and AEW indices are made for the Atlantic basin.

## 2.2 Data Processing

The HURDAT2 data is subjected to a filtering process to include only systems that reach 34 knots, which we define as cyclogenesis in each respective region. Three important datasets are then created. The first two are datasets of TS counts and a TS climatology (Fig. 2), and the third is a binary index that reflects whether TS genesis happened in a given week. Subsequently, a timeseries of TS genesis events per week is computed by aggregating the number of cyclogenesis events that happened within each region by calendar day and doing a rolling sum with a window of seven days to create the TS counts. To build the TS climatology, the TS counts are divided by 365 in

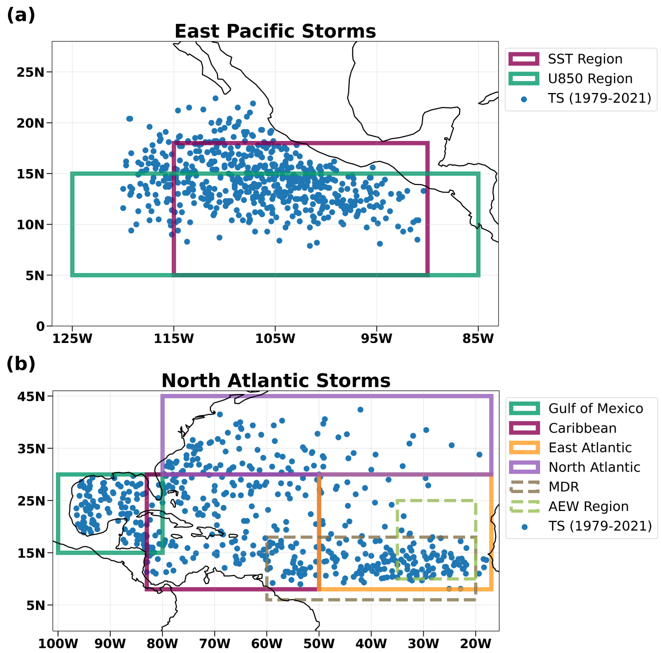

**Figure 2.1:** Location where storms reached cyclogenesis (34 knots) between 1979 to 2021. (a) East Pacific region ($5^\circ - 25^\circ$ N, $90^\circ - 120^\circ$ W); the two drawn boxes represent the regions used to create the SST ($5^\circ - 18^\circ$ N, $90^\circ - 115^\circ$ W) and U850 ($5^\circ - 15^\circ$ N, $85^\circ - 125^\circ$ W) indices. (b) As in (a) but for north Atlantic storms. The Gulf of Mexico is defined as the region between $15^\circ - 30^\circ$ N and $80^\circ - 100^\circ$ W. The Caribbean region extends from $8^\circ - 30^\circ$ N and $50^\circ - 100^\circ$ W. The west Atlantic is the addition of the Gulf of Mexico and the Caribbean. The east Atlantic is defined as $5^\circ - 30^\circ$ N and $18^\circ - 50^\circ$ W, and the north Atlantic is $30^\circ - 45^\circ$ N and $50^\circ - 80^\circ$ W. The regions enclosed in dashed lines are the Main Development Region ($5^\circ - 18^\circ$ N, $20^\circ - 60^\circ$ W) and the African Easterly Wave ($10^\circ - 25^\circ$ N, $20^\circ - 35^\circ$ W) index region.

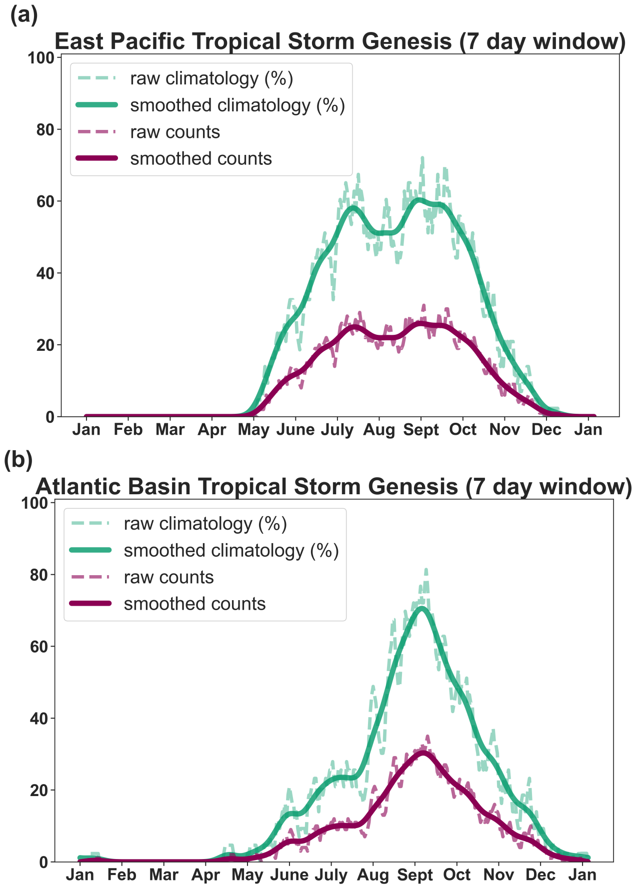

**Figure 2.2:** TS climatology and TS counts. The TS counts consists of all the storms that reached cyclogenesis added for each day of the year from 1979 to 2021. Solid lines are the smoothed climatology and counts, while the dashed lines are the corresponding raw data.

order to get TS genesis probabilities per week of the calendar year. To smooth the TS counts and the TS climatology, a forward-backward 1-2-1 filter is applied twenty times. These two curves are plotted as solid lines in Fig. 2, while their respective raw counts and probabilities are represented as dashed lines. The TS counts are the average number of cyclogenesis per week, while the TS climatology is the cyclogenesis probability per week. Finally, a binary index is also created from HURDAT data. To make the binary index, on days where storms reached to TS cyclogenesis a "1" is applied to the past and next three days in other to have a seven-day window of days when TS genesis was observed from 1979 to 2021. The remaining days get assigned a "0" to signify the lack of TS genesis on those days. This binary index is used as the label, and thus, act as the predictand for logistic regression and neural network prediction tasks.

Zonal wind data at 850-mb is obtained from the ERA5 Reanalysis and utilized to construct a zonal wind index (U850) for the east Pacific because of its relation to the enhancement or suppression of convection in this region (Maloney and Hartmann 2001). Zonal wind within the ranges of $5^\circ - 15^\circ$ N and $125^\circ - 85^\circ$ W is averaged by day, and the temporal mean over the entire set is subtracted to define anomalies. These anomalies are further detrended by calendar day to remove the multi-year trend. Similarly, SST data within the ranges of $5^\circ - 18^\circ$ N and $115^\circ - 90^\circ$ W is obtained from ERA5. SST in this region has been shown to covary with intraseasonal convection (Maloney et al. 2008). The same data processing approach used for the U850 index is applied to generate the SST index.

In the Atlantic region, an MDR SST index is created using SST data within the range of $5^\circ - 18^\circ$ N and $60^\circ - 20^\circ$ W. This data undergoes the same data processing steps as the U850 and SST indices for the east Pacific. Additionally, an AEW index is defined by averaging daily 700mb meridional winds over every grid point within $10^\circ - 25^\circ$ N, $35^\circ - 20^\circ$ W (Arnault and Roux 2011). The data is then passed through a fast Fourier transform, keeping only the high frequencies with periods less than 10 days associated with AEWs. Then, a rolling variance with a 10-day window is applied at each grid point in Fourier space. Finally, an area average is computed every day to produce the AEW activity index, whose timeseries is shown in Fig. S16.

## 2.3 Data-driven Models

Two data-driven machine learning models of different complexities are compared. First, binary logistic regression (LR) models are constructed to predict TS formation based on the input predictors for the east Pacific and the Atlantic basin. Binary logistic regression is a widely-used classification method that produces probability outputs by utilizing a sigmoid function as the activation function. Specifically, LR can be written as

$$P(Y|x) = \frac{e^{\beta_0+\beta_1 x_1+\beta_2 x_2+...+\beta_n x_n}}{1+e^{\beta_0+\beta_1 x_1+\beta_2 x_2+...+\beta_n x_n}}, \tag{2.1}$$

where $x_n$ are the predictor values, $Y$ is the event we want to predict, $P(Y|x)$ is the probability of $Y$ happening given $x$, $\beta_n$ are the regression coefficients, or the relationship between the predictand and the predictor values, and $i = 1, 2, 3, ...n$, where $n$ is the total number of predictors.

Additionally, neural networks (NN) are trained—one for the east Pacific and another for the Atlantic basin—to further increase the sophistication of the model and potentially enhance the predictive capabilities. The architecture of the NN involves passing the input features through two hidden layers comprising 25 nodes each (25 x 25) (Fig. 3). Moreover, the NN models utilize a hyperbolic tangent ($tanh$) activation function between the hidden layers and employs a softmax activation function in the output layer to obtain a binary result. The batch size for the NN is 32,

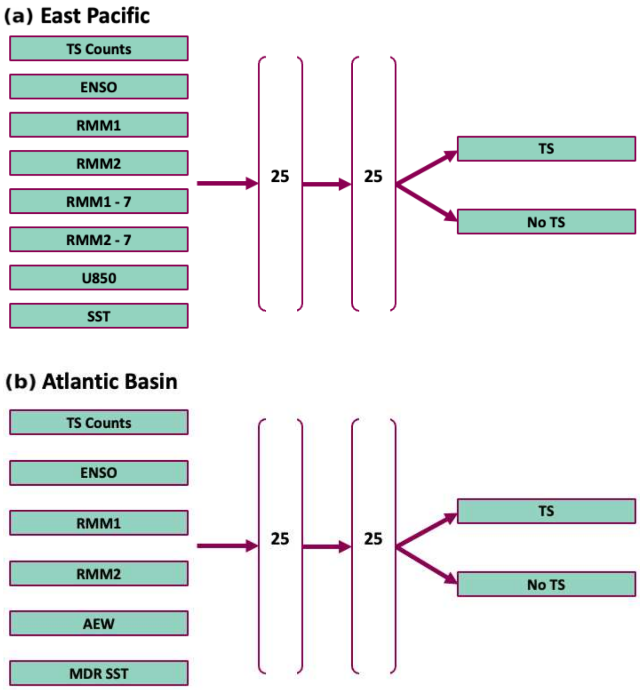

**Figure 2.3:** Neural network architectures for the two studied regions. (a) Architecture for the east Pacific where the input features are hurricane counts, ENSO, RMM1, RMM2, RMM1-7, RMM2-7, 850-mb zonal winds (U850), and SSTs. (b) Architecture for the Atlantic, the features are TS counts, ENSO, RMM1, RMM2, AEW, and MDR SST. For both networks the output is binary, “TS" or “No TS".

with a learning rate of 0.0003, and 30 epochs. The loss function applied is the binary crossentropy function. Appendix Table G.1 and G.2 shows the training loss values at 30 epochs for different architectures, demonstrating that the chosen architecture is the most optimal found for both regions.

AI explainability is applied to the NN through SHAP (Shapley Additive Explanations) values (Lundberg and Lee 2016) to quantify the variable importances for the models. Positive SHAP values indicate features that are driving the model towards forecasting TS genesis, while negative SHAP values indicate features that drive the model towards forecasting no TS genesis.

Given the small sample size used in this study (limited to storms from 1979 to 2021, 691 for the east Pacific and 554 for the North Atlantic), we do not have a separate testing dataset. Instead, a $k-$fold cross-validation approach is employed to assess the performance and generalizability of both the LR and NN models, and to maximize exposure to unseen data during training. $K-$fold cross-validation involves dividing the available data into $k$ subsets (or folds), where $k-1$ folds are used for model training and the remaining fold is used for validation. In this work, the data was randomly partitioned by year into seven folds, resulting in thirty-six years for training, and six for validation for each fold. By employing $k-$fold cross-validation, the models are evaluated using multiple independent subsets of training and validation data, which helps to assess their performance on unseen data. This approach ensures that the models developed are more robust, general, and capable of making accurate predictions beyond the data used for training.

## 2.4 Brier Skill Score

Here, we utilize the Brier skill score ($BSS$) as a measure of the predictive skill of our probabilistic forecasts. The Brier score ($BS$), upon which the Brier skill score is based, is defined as follows:

$$BS = \frac{1}{N}\sum_{t=1}^{N}(f_t - o_t)^2, \tag{2.2}$$

where $f_t$ represents the forecasted probability and $o_t$ represents the corresponding actual outcome at time $t$ (“0" or “1"). The Brier score quantifies the mean square error of the forecasted probabilities, with $N$ denoting the total number of forecast instances. The Brier skill score is then calculated by normalizing the Brier score with respect to a reference outcome forecast ($BS_{ref}$), specifically,

$$BSS = 1 - \frac{BS}{BS_{ref}}. \tag{2.3}$$

The $BS_{ref}$ for our models is the average number of times the binary index has “1" for a given calendar week. The Brier skill score ranges from 1 to 0, where a score of 1 indicates a perfect forecast and a score of 0 represents the skill of the reference forecast. Negative values indicate that the performance is worse than the reference.

# Chapter 3

# Results

## 3.1 East Pacific

In this work we use logistic regression (LR) and neural networks (NN) to increase the model complexity relative to past works. The inputs used include climate information pertaining to ENSO and MJO, as well as local SSTs and winds. We assess the models' performance using the Brier skill score, and apply AI explainability to further understand how each feature contributes to the NN's results. Fig.4a shows the Brier skill scores for the LR and NN models when the input features are TS counts, ENSO, RMM1, RMM2, RMM1-7, RMM2-7, SST, and U850. The dashed lines in Fig. 4 represent the mean Brier skill score per leadtime for the TS counts and reflects the climatology for each region which serves as the baseline for every model respectively. Both LR and NN models for the east Pacific exceed the respective baselines out to 21 days, when the Brier skill scores converges with the models' baselines. The NN has higher scores throughout all the leadtimes relative to the LR model, successfully improving upon past works that have used LR to forecast hurricane activity (e.g. Leroy and Wheeler 2008; Henderson and Maloney 2013). The forecasting skill for each model is measured by quantifying how much improvement the addition of features has over the baseline. Because we are applying k-fold cross-validation, every fold gets used once as validation set. The Brier skill score obtained when these folds are used as validation for input features TS counts, ENSO, RMM1, RMM2, RMM1-7, RMM2-7, SST, and U850 are shown as (seven) circles per leadtime in Fig.4a. If a validation fold achieved greater Brier skill

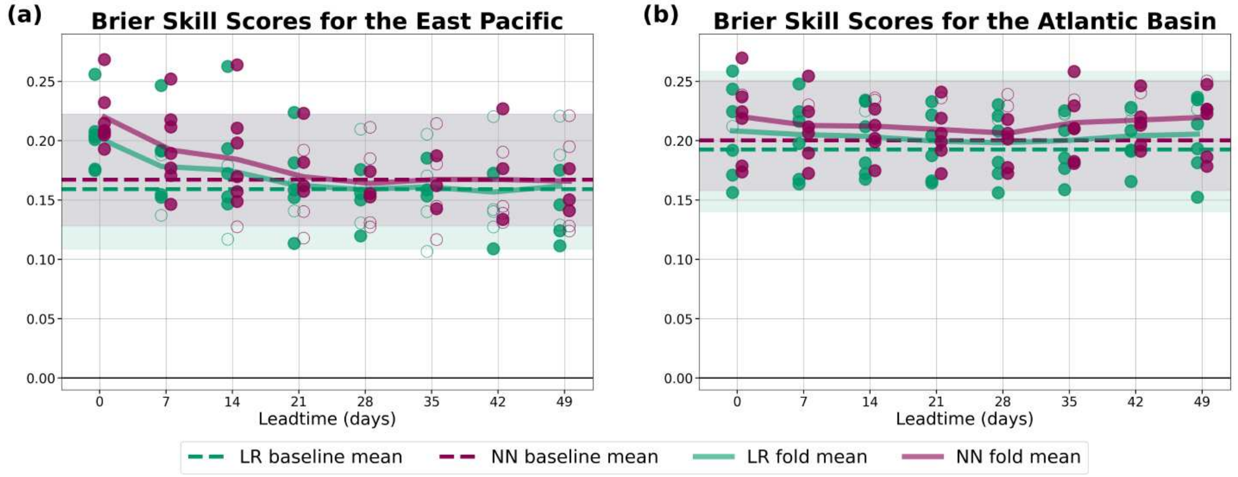

**Figure 3.1:** Brier skill score for the logistic regression and the neural network as a function of leadtime. Closed circles indicate the folds that scored higher than the baseline, while the open circles indicate the folds with scores lower than the baseline. (a) East Pacific brier skill scores for the LR and NN model when the input features are the TS counts, ENSO, RMM1, RMM2, RMM1-7, RMM2-7, SST, and U850. (b) Comparing the Atlantic basin LR and NN scores using as input the TS counts, ENSO, RMM1, RMM2, MDR SST, and AEW.

score than its respective baseline, it is shown as a closed circle. On the other hand, validation folds that obtained a Brier skill score lower than their baseline are shown as open circles. Since the goal is for every validation fold to beat its baseline, it is worth noting how for the east Pacific the NN is able to retain a greater number of folds with skill over the baseline throughout the first three weeks relative to the LR (Fig.4a).

In addition to using TS counts, ENSO, RMM1, RMM2, RMM1-7, RMM2-7, SST, and U850 as input features, we retrain our NN model to explore a variety of feature combinations. Fig. 5a shows the Brier skill score differences from the baseline, representing how much the model improves when features other than TS counts are included. When the east Pacific model has only TS counts and ENSO information, the Brier skill scores are nearly identical to the scores for the baseline (Fig.5a; shown as teal dots). This suggests that adding only ENSO over the baseline for the east Pacific does not provide the model additional information that it can use to create better predictions. When the input includes TS counts, ENSO, RMM1 and RMM2, the model is able to use the combination of ENSO and MJO information to further improve the predictive abilities (Fig.5a; shown as yellow dots). When TS counts, RMM1, and RMM2 are used as the input features, the model shows improvement over the baseline at 21 days leadtime (Fig.5a; shown as burgundy dots). Finally, when the model includes TS counts, ENSO, RMM1, RMM2, RMM1-7, RMM2-7 it achieves even higher Brier skill scores for the east Pacific, enabling the model to have greater improvement over the baseline to three weeks into the future (Fig.5a; shown as purple dots). This last feature combination includes more information about the evolution of the MJO. Having past RMM information tells the model the phase the MJO was previously in, and RMM1 and RMM2 tells the model the phase it is currently in. The lagged RMMs provide information regarding the speed at which the MJO is traveling along the Pacific equator, in additon to other information such as the evolution of amplitude. The NN model identifies MJO indices as highly valuable for predicting cyclogenesis, consistent with existing literature that establishes clear associations between MJO and east Pacific tropical cyclone activity (Maloney and Hartmann 2000). The inclusion of SST and U850 to ENSO, RMM1, RMM2, RMM1-7, and RMM2-7 provide additional information for the NN, hence it obtains highest Brier skill score amongst all tested feature combinations (Fig.5a).

To showcase the model's capabilities, the probability of cyclogenesis generated by the NN for each week of the 1983 hurricane season in the east Pacific is plotted as dots in Fig. 6a and 6c, and compared with the observed cyclogenesis weeks (shaded regions on Fig. 6a and 6c). Looking at Fig.6a, one can see that the NN generally increases the TS genesis probabilities when cyclogenesis was observed, demonstrating its ability to capture real occurrences. To gain insight into the model's decision-making process, an analysis using SHAP values for each variable is presented in Fig. 6b. The SHAP values indicate the influence each feature has on the NN's predictions, with positive values indicating variables that push predictions toward TS genesis predictions, and negative values indicating features that decrease the chances for TS genesis.

Throughout the hurricane season, the TS counts, which serve as a measure of TS climatology, consistently display high positive SHAP values (Fig.6b), panel 1 as expected since it shows that the historical frequency of TSs strongly influences the model's predictions. The other variables change from day to day and provide prediction skill beyond the region's reference. During mid-June, RMM1 and RMM1-7 exhibited positive SHAP values, coinciding with spikes in TS development probabilities when TC Barbara went through cyclogenesis (Fig.6b, panel 2). Moreover, during mid-June the MJO was in Phase 2, which is associated with a higher TS activity in the east Pacific (Maloney and Hartmann 2000). Not only was the MJO in a favorable phase for east Pacific cyclogenesis during mid-June, but the local SSTs also experienced the highest values during this period. Phase 2 is also observed in early September and mid-October (Fig. S17), which coincide with events of higher probabilities in Fig.6a and the cyclogenesis of TCs Kiko and Tico. Moreover, the 850-mb zonal winds were westerlies (Fig. S20), which are associated with enhanced TC activity in the east Pacific (Maloney and Hartmann 2000). Fig. 6b shows how the NN model assigns higher SHAP values during these two cyclogenesis events, demonstrating that the model identified the relationship between TC genesis and the 850-mb zonal wind direction in the east Pacific. During early-August and November, the MJO was in Phases 3-6 (Fig. S17) and the NN assigns low TS genesis probabilities (Fig. 6a). U850 has three events in Fig.6b, panel 4 where the SHAP values are negative, during late-June, early-September, and early to mid-October. During these three events, the U850 values were anomalous easterly, which have been shown to suppress TS genesis in the east Pacific (Maloney and Hartmann 2000).

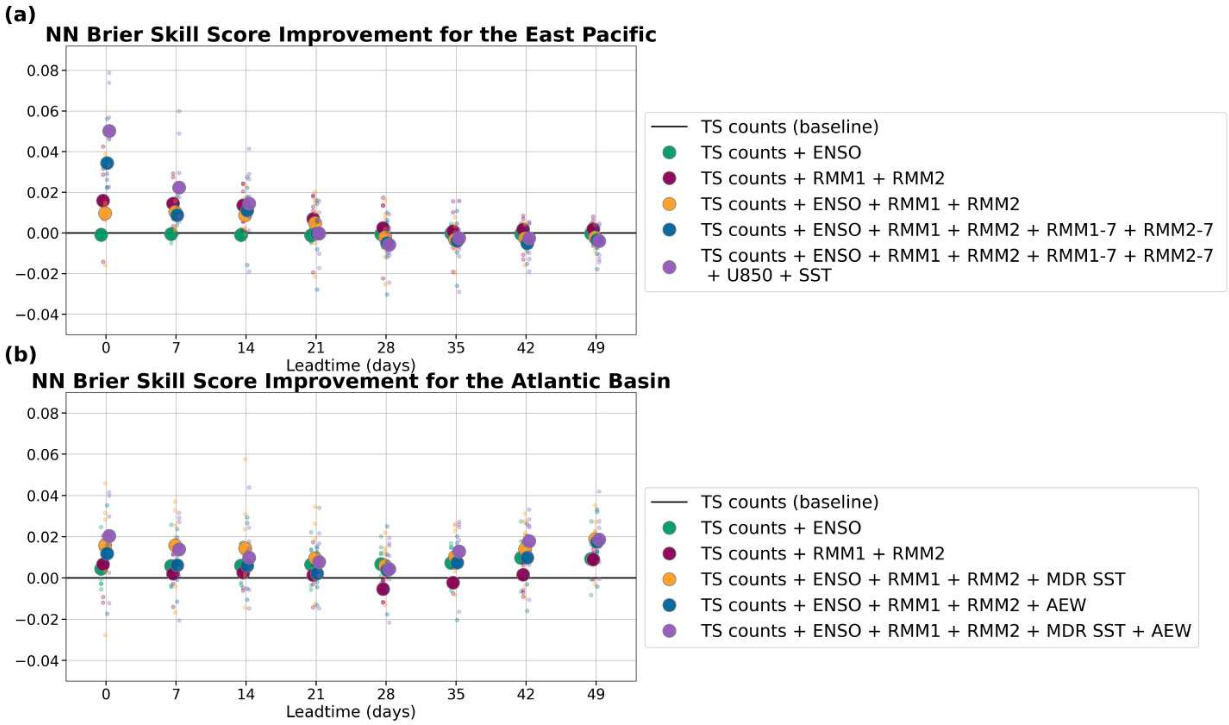

**Figure 3.2:** Brier skill scores and Brier skill score differences from the baseline for the NN models for the east Pacific and the Atlantic basin using different feature combinations. (a) NN Brier skill scores and Brier skill score differences for the east Pacific. (b) NN Brier skill scores and brier skill score differences for the Atlantic basin.

## 3.2 Atlantic Basin

Across all Atlantic subregions, the NN model consistently outperforms the LR model (Fig. 4b, Fig. S6 - S10). The LR model for the Atlantic incorporating TS counts, ENSO, RMM1, RMM2, AEW, and MDR SST demonstrates improved performance in the weekly folds compared to their respective baselines and demonstrates skill relative to the climatology baseline for at least two weeks (Fig. 4b). The NN model yields higher Brier skill scores than LR for the Atlantic basin as a whole and its subregions because of its increased complexity. Moreover, over half of the folds exhibit scores surpassing their respective baselines throughout most of the forecast period (Fig. 4b). It is evident that the inclusion of additional features beyond the baseline provide valuable information for the model. Incorporating ENSO and MJO information results in an improved performance of the NN model (Fig.5b). Furthermore, the addition of MDR SST further enhances the forecasting skill. MDR SST is a valuable variable to include since it provides SST information in the region where most systems undergo cyclogenesis (Fig.5b) (Mann and Emanuel 2006, Elsner 2006). The inclusion of AEW increases skill during the first week.

We have also examined predictions for sub-basins of the Atlantic. While we cannot go into extensive detail here, forecast models for these sub-basins produce some notable successes. For example, TC activity in the Gulf of Mexico, the Caribbean, and the region comprised by adding these two, referred as “west Atlantic" benefit from the RMM indices because of the direct influence the MJO has over the region (Maloney and Hartmann 2000b). Furthermore, the Gulf of Mexico shows Brier skill score improvement when either the MDR SSTs or the AEW index are included in addition to TS counts, ENSO, RMM1, and RMM2 (Fig. S11). The Caribbean, benefits from the addition of both, the MDR SSTs and the EAW index, along with TS counts, ENSO, RMM1, and RMM2, obtaining higher Brier skill scores than without them (Fig. S12). Finally, the west Atlantic results in higher Brier skill scores when MDR SSTs and AEW index are added to TS counts, ENSO, RMM1, and RMM2 for the first two weeks (Fig. S13). Three weeks onward, the model stops learning from the AEW index and relies only on the addition of MDR SSTs.

Examining the year 2021 for the Atlantic basin, it is apparent that most of the peaks in the predictions align with the weeks with observed cyclogenesis (Fig.6c). Further analysis reveals that the model relies on ENSO, MJO, and the local data that contributes to variability observed during the hurricane season (Fig.6d). When TC Grace went through cyclogenesis, the AEW reached its highest influence for the hurricane season (Fig. S27). Our network was able to find this pattern and is reflected in Fig. 6b panel 4, where the AEW has a positive SHAP value. TC Ida experienced cyclogenesis around late August, and according to Fig.6b, the features that positively influenced the model during that time are the TS climatology and ENSO. During late August the TS counts reach the highest value (Fig. 3b), and also ENSO starts to settle into La Niña phase (Fig. S24), both good indicators for high cylogenesis probability (Klotzbach and Oliver 2015). Moreover, the AEW index (Fig. S28) was high and the MJO was in phase 2 (Fig. **??**23). Finally, looking at TC Sam, the moment this storm went through cyclogenesis the MJO was in phase 4 (Fig. S23), which is unfavorable for TC activity in the Atlantic (Klotzbach and Oliver 2015), and the assigned SHAP values are negative. Because of La Niña, both ENSO and TS counts push the model towards high cyclogenesis probabilities during this period (Fig. 6c) reflected in positive SHAP values (Fig. 6d). The MDR SSTs were below average for the 2021 hurricane season (Fig. S28) and this causes the NN to reduce its prediction of TC activity, as seen in the negative SHAP values (Fig.6d, panel 4).

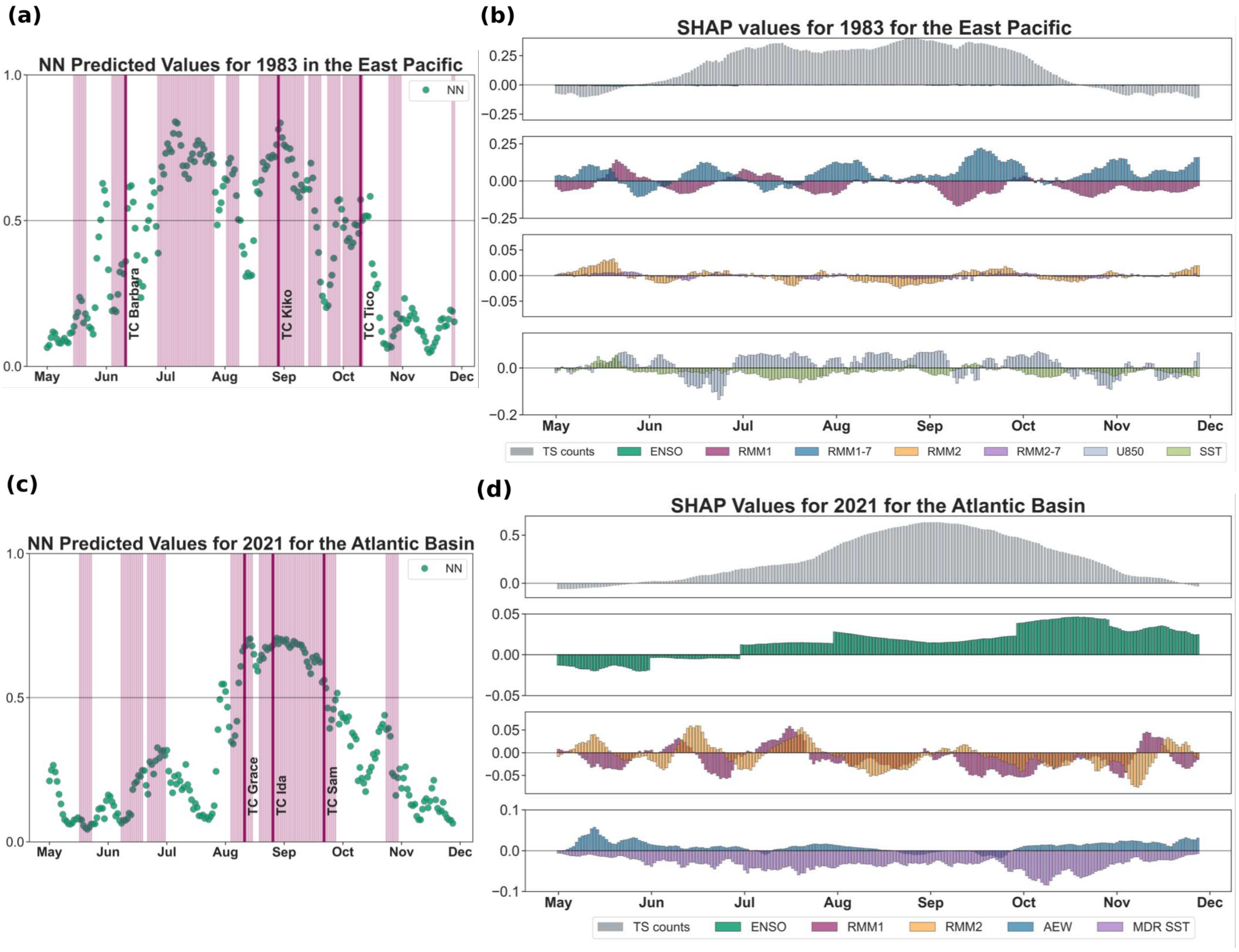

**Figure 3.3:** Predicted probabilities by the neural network and the associated SHAP values. (a,c) The circles indicate the TS genesis probabilities per week during the hurricane season, and the shaded lines are the weeks where cyclogenesis was observed. Darker lines represent cyclogenesis days for some storms that reached at least 96 knots. (b,d) The SHAP values for he NN. Features with positive SHAP values pushed the model towards forecasting cyclogenesis that week, while variables with negative SHAP values pushed the model towards a forecast of no cyclogenesis. Note the different y-axis limits for the top panels of (b) and (d).

# Chapter 4

# Conclusion

In this study, logistic regression (LR) and neural network (NN) TS genesis forecast models are built for the east Pacific and Atlantic. The models utilize climate and environmental data as inputs, including ENSO, MJO, SST and local winds. To evaluate the models' performance, the Brier skill score is computed for each model at various lead times. The TS counts, representing the TS climatology, serve as the baseline for the LR and NN models. Generally, both models exhibit improved performance when additional information is incorporated beyond the baseline. Moreover, the NN model achieves higher Brier skill scores compared to the LR model, indicating that increased sophistication leads to greater forecasting skill. In the east Pacific, the optimal feature combination for the models includes ENSO, RMM1, RMM2, RMM1-7, RMM2-7, U850, and SST indices. By including these indices as inputs, both the LR and NN models demonstrate forecasting skill for up to three weeks into the future. In the Atlantic basin, the optimal feature combination consists of ENSO, RMM1, RMM2, MDR SST, and AEW indices and enable the NN model to retain forecasting skill for up to four weeks into the future, more than when the LR is used. When the Atlantic basin is divided into subregions the Brier skill scores are lower than those for the entire basin likely due to a reduction in sample size resulting from the subsectioning of the Atlantic. Nonetheless, west Atlantic subregions benefit from MJO information and are further improved by including the MDR SSTs and the AEW index.

The objective of this research was to build upon previous work on data-driven hurricane prediction that utilized ENSO and MJO data by including additional local environmental information and comparing NN and LR models to make forecasts of TC activity at S2S leadtimes. Comparing both models, the NN produced higher Brier skill scores as a function of leadtime relative the results obtained using LR. Our NN models demonstrate forecasting skill for up to three weeks into the future in the east Pacific, and up to four weeks in the Atlantic basin, exploiting the relationships between ENSO and MJO with TS activity in the east Pacific and Atlantic. Moreover, the local environmental variables (winds and SSTs) further increase the magnitude of the Brier skill scores of the models as a function of leadtime since this addition creates a more robust forecasting model. A key revelation in this study centers on the incorporation of AI explainability techniques, specifically the utilization of SHAP values, to dissect the role and impact of the input variables within our models. This methodology gives us a framework to discern precisely which variables hold sway over the model's decision-making processes at distinct points in time.

# Chapter 5

# Future Works

In future studies, a more sophisticated AEW index might be used, such as one that identifies individual disturbances. AEW strength, along with environmental conditions, have been proven to be good TC activity indicators (Bercos-Hickey et al. 2023). Additionally, there is evidence of teleconnections between Atlantic SSTs and eastern Pacific TCs (Patricola et al. 2016), hence the inclusion of Atlantic SSTs into east Pacific models is worth exploring. Finally, the addition of other input variables, such as the Atlantic Meridional Mode, North Atlantic Oscillation, and the Quasi-Biennial Oscillation may further enhance the results.

# Chapter 6

# Bibliography

Adames, Á. F. (2021). Interactions between Water Vapor, Potential Vorticity, and Vertical Wind Shear in Quasi-Geostrophic Motions: Implications for Rotational Tropical Motion Systems. Journal of the Atmospheric Sciences, 78(3), 903–923. https://doi.org/10.1175/JAS-D-20-0205.1

Anthes, R. A., Kuo, Y.-H., Benjamin, S. G., & Li, Y.-F. (1982). The Evolution of the Mesoscale Environment of Severe Local Storms: Preliminary Modeling Results. Monthly Weather Review, 110(9), 1187–1213. https://doi.org/10.1175/1520-0493(1982)110<1187:TEOTME>2.0.CO;2

Arnault, J., & Roux, F. (2011). Characteristics of African easterly waves associated with tropical cyclogenesis in the Cape Verde Islands region in July-August-September of 2004-2008. Atmospheric Research, 100(1), 61–82. https://doi.org/10.1016/j.atmosres.2010.12.028

Belanger, J. I., Curry, J. A., & Webster, P. J. (2010). Predictability of North Atlantic Tropical Cyclone Activity on Intraseasonal Time Scales. Monthly Weather Review, 138(12), 4362–4374. https://doi.org/10.1175/2010MWR3460.1

Bell, G. D., & Chelliah, M. (2006a). Leading Tropical Modes Associated with Interannual and Multidecadal Fluctuations in North Atlantic Hurricane Activity. Journal of Climate, 19(4), 590–612. https://doi.org/10.1175/JCLI3659.1

Bell, G. D., & Chelliah, M. (2006b). Leading Tropical Modes Associated with Interannual and Multidecadal Fluctuations in North Atlantic Hurricane Activity. Journal of Climate, 19(4), 590–612. https://doi.org/10.1175/JCLI3659.1

Bercos-Hickey, E., Patricola, C. M., Loring, B., & Collins, W. D. (2023). The Relationship Between African Easterly Waves and Tropical Cyclones in Historical and Future Climates in the HighResMIP-PRIMAVERA Simulations. Journal of Geophysical Research: Atmospheres, 128(7), e2022JD037471. https://doi.org/10.1029/2022JD037471

Bister, M., & Emanuel, K. A. (1998). Dissipative heating and hurricane intensity. Meteorology and Atmospheric Physics, 65(3–4), 233–240. https://doi.org/10.1007/BF01030791

Burpee, R. W. (1972). The Origin and Structure of Easterly Waves in the Lower Troposphere of North Africa. Journal of the Atmospheric Sciences, 29(1), 77–90. https://doi.org/10.1175/1520-0469(1972)029<0077:TOASOE>2.0.CO;2

C. L. Chan, J., Shi, J., & Liu, K. S. (2001). Improvements in the Seasonal Forecasting of Tropical Cyclone Activity over the Western North Pacific. Weather and Forecasting, 16(4), 491–498. https://doi.org/10.1175/1520-0434(2001)016<0491:IITSFO>2.0.CO;2

Camargo, S. J., Wheeler, M. C., & Sobel, A. H. (2009). Diagnosis of the MJO Modulation of Tropical Cyclogenesis Using an Empirical Index. Journal of the Atmospheric Sciences, 66(10), 3061–3074. https://doi.org/10.1175/2009JAS3101.1

Collins, J. (2007). The Relationship of ENSO and Relative Humidity to Interannual Variations of Hurricane Frequency in the North-East Pacific Ocean.

https://www.semanticscholar.org/paper/The-Relationship-of-ENSO-and-Relative-Humidity-to-Collins/cb7fab7f953dd0c83cdc481b6865757afa176440

Collins, J. M., & Mason, I. M. (2000). Local environmental conditions related to seasonal tropical cyclone activity in the northeast Pacific Basin. Geophysical Research Letters, 27(23), 3881–3884. https://doi.org/10.1029/2000GL011614

Diedhiou, A., Janicot, S., Viltard, A., De Felice, P., & Laurent, H. (1999). Easterly wave regimes and associated convection over West Africa and tropical Atlantic: results from the NCEP/NCAR and ECMWF reanalyses. Climate Dynamics, 15(11), 795–822. https://doi.org/10.1007/s003820050316

Elsner, J. B. (2006). Evidence in support of the climate change–Atlantic hurricane hypothesis. Geophysical Research Letters, 33(16). https://doi.org/10.1029/2006GL026869

Emanuel, K. (2005). Increasing destructiveness of tropical cyclones over the past 30 years. Nature, 436(7051), 686–688. https://doi.org/10.1038/nature03906

Emanuel, K. A. (1994). Atmospheric convection. Oxford University Press, USA.

Fink, A. H., & Reiner, A. (2003). Spatiotemporal variability of the relation between African Easterly Waves and West African Squall Lines in 1998 and 1999. Journal of Geophysical Research, 108(D11), 4332. https://doi.org/10.1029/2002JD002816

Goldenberg, S. B., Landsea, C. W., Mestas-Nuñez, A. M., & Gray, W. M. (2001a). The Recent Increase in Atlantic Hurricane Activity: Causes and Implications. Science, 293(5529), 474–479. https://doi.org/10.1126/science.1060040

Goldenberg, S. B., Landsea, C. W., Mestas-Nuñez, A. M., & Gray, W. M. (2001b). The Recent Increase in Atlantic Hurricane Activity: Causes and Implications. Science, 293(5529), 474–479. https://doi.org/10.1126/science.1060040

Goldenberg, S. B., & Shapiro, L. J. (1996). Physical Mechanisms for the Association of El Niño and West African Rainfall with Atlantic Major Hurricane Activity. Journal of Climate, 9(6), 1169–1187. https://doi.org/10.1175/1520-0442(1996)009<1169:PMFTAO>2.0.CO;2

Gray, W. M. (1984a). Atlantic Seasonal Hurricane Frequency. Part I: El Niño and 30 mb Quasi-Biennial Oscillation Influences. Monthly Weather Review, 112(9), 1649–1668. https://doi.org/10.1175/1520-0493(1984)112<1649:ASHFPI>2.0.CO;2

Gray, W. M. (1984b). Atlantic Seasonal Hurricane Frequency. Part II: Forecasting its Variability. Monthly Weather Review, 112(9), 1669–1683. https://doi.org/10.1175/1520-0493(1984)112<1669:ASHFPI>2.0.CO;2

Henderson, S. A., & Maloney, E. D. (2013a). An Intraseasonal Prediction Model of Atlantic and East Pacific Tropical Cyclone Genesis. Monthly Weather Review, 141(6), 1925–1942. https://doi.org/10.1175/MWR-D-12-00268.1

Henderson, S. A., & Maloney, E. D. (2013b). An Intraseasonal Prediction Model of Atlantic and East Pacific Tropical Cyclone Genesis. Monthly Weather Review, 141(6), 1925–1942. https://doi.org/10.1175/MWR-D-12-00268.1

Hersbach, H., Bell, B., Berrisford, P., Hirahara, S., Horányi, A., Muñoz-Sabater, J., Nicolas, J., Peubey, C., Radu, R., Schepers, D., Simmons, A., Soci, C., Abdalla, S., Abellan, X., Balsamo, G., Bechtold, P., Biavati, G., Bidlot, J., Bonavita, M., … Thépaut, J. (2020a). The

ERA5 global reanalysis. Quarterly Journal of the Royal Meteorological Society, 146(730), 1999–2049. https://doi.org/10.1002/qj.3803

Hersbach, H., Bell, B., Berrisford, P., Hirahara, S., Horányi, A., Muñoz-Sabater, J., Nicolas, J., Peubey, C., Radu, R., Schepers, D., Simmons, A., Soci, C., Abdalla, S., Abellan, X., Balsamo, G., Bechtold, P., Biavati, G., Bidlot, J., Bonavita, M., … Thépaut, J. (2020b). The ERA5 global reanalysis. Quarterly Journal of the Royal Meteorological Society, 146(730), 1999–2049. https://doi.org/10.1002/qj.3803

Hersbach, H., Bell, B., Berrisford, P., Hirahara, S., Horányi, A., Muñoz-Sabater, J., Nicolas, J., Peubey, C., Radu, R., Schepers, D., Simmons, A., Soci, C., Abdalla, S., Abellan, X., Balsamo, G., Bechtold, P., Biavati, G., Bidlot, J., Bonavita, M., … Thépaut, J. (2020c). The ERA5 global reanalysis. Quarterly Journal of the Royal Meteorological Society, 146(730), 1999–2049. https://doi.org/10.1002/qj.3803

Hopsch, S. B., Thorncroft, C. D., & Tyle, K. R. (2010a). Analysis of African Easterly Wave Structures and Their Role in Influencing Tropical Cyclogenesis. Monthly Weather Review, 138(4), 1399–1419. https://doi.org/10.1175/2009MWR2760.1

Hopsch, S. B., Thorncroft, C. D., & Tyle, K. R. (2010b). Analysis of African Easterly Wave Structures and Their Role in Influencing Tropical Cyclogenesis. Monthly Weather Review, 138(4), 1399–1419. https://doi.org/10.1175/2009MWR2760.1

Kiladis, G. N., Thorncroft, C. D., & Hall, N. M. J. (2006). Three-Dimensional Structure and Dynamics of African Easterly Waves. Part I: Observations. Journal of the Atmospheric Sciences, 63(9), 2212–2230. https://doi.org/10.1175/JAS3741.1

Kim, H.-M., Webster, P. J., & Curry, J. A. (2011). Modulation of North Pacific Tropical Cyclone Activity by Three Phases of ENSO. Journal of Climate, 24(6), 1839–1849. https://doi.org/10.1175/2010JCLI3939.1

Klotzbach, P. J. (2014). The Madden–Julian Oscillation's Impacts on Worldwide Tropical Cyclone Activity. Journal of Climate, 27(6), 2317–2330. https://doi.org/10.1175/JCLI-D-13-00483.1

Klotzbach, P. J., & Oliver, E. C. J. (2015). Modulation of Atlantic Basin Tropical Cyclone Activity by the Madden–Julian Oscillation (MJO) from 1905 to 2011. Journal of Climate, 28(1), 204–217. https://doi.org/10.1175/JCLI-D-14-00509.1

Landsea, C., Franklin, J., & Beven, J. (2015). The revised Atlantic hurricane database (HURDAT2). NOAA/NHC.[Available Online at Nhc. Noaa. Gov.].

Landsea, C. W. (1993). A Climatology of Intense (or Major) Atlantic Hurricanes. Monthly Weather Review, 121(6), 1703–1713. https://doi.org/10.1175/1520-0493(1993)121<1703:ACOIMA>2.0.CO;2

Lee, C.-Y., Camargo, S. J., Vitart, F., Sobel, A. H., & Tippett, M. K. (2018a). Subseasonal Tropical Cyclone Genesis Prediction and MJO in the S2S Dataset. Weather and Forecasting, 33(4), 967–988. https://doi.org/10.1175/WAF-D-17-0165.1

Lee, C.-Y., Camargo, S. J., Vitart, F., Sobel, A. H., & Tippett, M. K. (2018b). Subseasonal Tropical Cyclone Genesis Prediction and MJO in the S2S Dataset. Weather and Forecasting, 33(4), 967–988. https://doi.org/10.1175/WAF-D-17-0165.1

Leroy, A., & Wheeler, M. C. (2008). Statistical Prediction of Weekly Tropical Cyclone Activity in the Southern Hemisphere. Monthly Weather Review, 136(10), 3637–3654. https://doi.org/10.1175/2008MWR2426.1

Lundberg, S., & Lee, S.-I. (2017). A Unified Approach to Interpreting Model Predictions. https://doi.org/10.48550/ARXIV.1705.07874

Madden, R. A., & Julian, P. R. (1971). Detection of a 40–50 Day Oscillation in the Zonal Wind in the Tropical Pacific. Journal of the Atmospheric Sciences, 28(5), 702–708. https://doi.org/10.1175/1520-0469(1971)028<0702:DOADOI>2.0.CO;2

Madden, R. A., & Julian, P. R. (1972). Description of Global-Scale Circulation Cells in the Tropics with a 40–50 Day Period. Journal of the Atmospheric Sciences, 29(6), 1109–1123. https://doi.org/10.1175/1520-0469(1972)029<1109:DOGSCC>2.0.CO;2

Maloney, E. D., & Hartmann, D. L. (2000a). Modulation of Hurricane Activity in the Gulf of Mexico by the Madden-Julian Oscillation. Science, 287(5460), 2002–2004. https://doi.org/10.1126/science.287.5460.2002

Maloney, E. D., & Hartmann, D. L. (2000b). Modulation of Eastern North Pacific Hurricanes by the Madden–Julian Oscillation. Journal of Climate, 13(9), 1451–1460. https://doi.org/10.1175/1520-0442(2000)013<1451:MOENPH>2.0.CO;2

Maloney, E. D., & Shaman, J. (2008). Intraseasonal Variability of the West African Monsoon and Atlantic ITCZ. Journal of Climate, 21(12), 2898–2918. https://doi.org/10.1175/2007JCLI1999.1

Mann, M. E., & Emanuel, K. A. (2006). Atlantic hurricane trends linked to climate change. Eos, Transactions American Geophysical Union, 87(24), 233–241. https://doi.org/10.1029/2006EO240001

Muñoz-Sabater, J., Dutra, E., Agustı-Panareda, A., Albergel, C., Arduini, G., Balsamo, G., Boussetta, S., Choulga, M., Harrigan, S., Hersbach, H., Martens, B., Miralles, D. G., Piles, M., Rodrıguez-Fernández, N. J., Zsoter, E., Buontempo, C., & Thépaut, J.-N. (2021). ERA5-Land: a state-of-the-art global reanalysis dataset for land applications. Earth System Science Data, 13(9), 4349–4383. https://doi.org/10.5194/essd-13-4349-2021

NCEI. (2023). 2023 Global Climate Report | National Centers for Environmental Information (NCEI). https://www.ncei.noaa.gov/access/monitoring/monthly-report/global/202300

Palmen, E. (1948). On the formation and structure of tropical hurricanes. Geophysica, 3(1), 26–38.

Pasch, R. J., Avila, L. A., & Jiing, J.-G. (1998). Atlantic Tropical Systems of 1994 and 1995: A Comparison of a Quiet Season to a Near-Record-Breaking One. Monthly Weather Review, 126(5), 1106–1123. https://doi.org/10.1175/1520-0493(1998)126<1106:ATSOAA>2.0.CO;2

Patricola, C. M., Saravanan, R., & Chang, P. (2017). A teleconnection between Atlantic sea surface temperature and eastern and central North Pacific tropical cyclones. Geophysical Research Letters, 44(2), 1167–1174. https://doi.org/10.1002/2016GL071965

Pytharoulis, I., & Thorncroft, C. (1999). The Low-Level Structure of African Easterly Waves in 1995. Monthly Weather Review, 127(10), 2266–2280. https://doi.org/10.1175/1520-0493(1999)127<2266:TLLSOA>2.0.CO;2

Rayner, N. A. (2003a). Global analyses of sea surface temperature, sea ice, and night marine air temperature since the late nineteenth century. Journal of Geophysical Research, 108(D14), 4407. https://doi.org/10.1029/2002JD002670

Rayner, N. A. (2003b). Global analyses of sea surface temperature, sea ice, and night marine air temperature since the late nineteenth century. Journal of Geophysical Research, 108(D14), 4407. https://doi.org/10.1029/2002JD002670

Rayner, N. A. (2003c). Global analyses of sea surface temperature, sea ice, and night marine air temperature since the late nineteenth century. Journal of Geophysical Research, 108(D14), 4407. https://doi.org/10.1029/2002JD002670

Reed, R. J., Norquist, D. C., & Recker, E. E. (1977). The Structure and Properties of African Wave Disturbances as Observed During Phase III of GATE. Monthly Weather Review, 105(3), 317–333. https://doi.org/10.1175/1520-0493(1977)105<0317:TSAPOA>2.0.CO;

Saunders, M. A., & Lea, A. S. (2005). Seasonal prediction of hurricane activity reaching the coast of the United States. Nature, 434(7036), 1005–1008. https://doi.org/10.1038/nature03454

Schlesinger, M. E., & Ramankutty, N. (1994). An oscillation in the global climate system of period 65–70 years. Nature, 367(6465), 723–726. https://doi.org/10.1038/367723a0

Service, C. C. C. (2019). ERA5-Land hourly data from 2001 to present. ECMWF. https://doi.org/10.24381/CDS.E2161BAC

Shaman, J., Esbensen, S. K., & Maloney, E. D. (2009). The Dynamics of the ENSO–Atlantic Hurricane Teleconnection: ENSO-Related Changes to the North African–Asian Jet Affect Atlantic Basin Tropical Cyclogenesis. Journal of Climate, 22(9), 2458–2482. https://doi.org/10.1175/2008JCLI2360.1

Thorncroft, C. D., & Hoskins, B. J. (1994). An idealized study of African easterly waves. I: A linear view. Quarterly Journal of the Royal Meteorological Society, 120(518), 953–982. https://doi.org/10.1002/qj.49712051809

Thorncroft, C., & Hodges, K. (2001). African Easterly Wave Variability and Its Relationship to Atlantic Tropical Cyclone Activity. Journal of Climate, 14(6), 1166–1179. https://doi.org/10.1175/1520-0442(2001)014<1166:AEWVAI>2.0.CO;2

Vecchi, G. A., & Knutson, T. R. (2008). On Estimates of Historical North Atlantic Tropical Cyclone Activity*. Journal of Climate, 21(14), 3580–3600. https://doi.org/10.1175/2008JCLI2178.1

Vecchi, G. A., Swanson, K. L., & Soden, B. J. (2008). Whither Hurricane Activity? Science, 322(5902), 687–689. https://doi.org/10.1126/science.1164396

Vitart, F., Ardilouze, C., Bonet, A., Brookshaw, A., Chen, M., Codorean, C., Déqué, M., Ferranti, L., Fucile, E., Fuentes, M., Hendon, H., Hodgson, J., Kang, H.-S., Kumar, A., Lin, H., Liu, G., Liu, X., Malguzzi, P., Mallas, I., … Zhang, L. (2017). The Subseasonal to Seasonal (S2S) Prediction Project Database. Bulletin of the American Meteorological Society, 98(1), 163–173. https://doi.org/10.1175/BAMS-D-16-0017.1

Wheeler, M. C., & Hendon, H. H. (2004). An All-Season Real-Time Multivariate MJO Index: Development of an Index for Monitoring and Prediction. Monthly Weather Review, 132(8), 1917–1932. https://doi.org/10.1175/1520-0493(2004)132<1917:AARMMI>2.0.CO;2(N.d.).

# Appendix A

# TC Counts and climatologies for the Atlantic Subregions

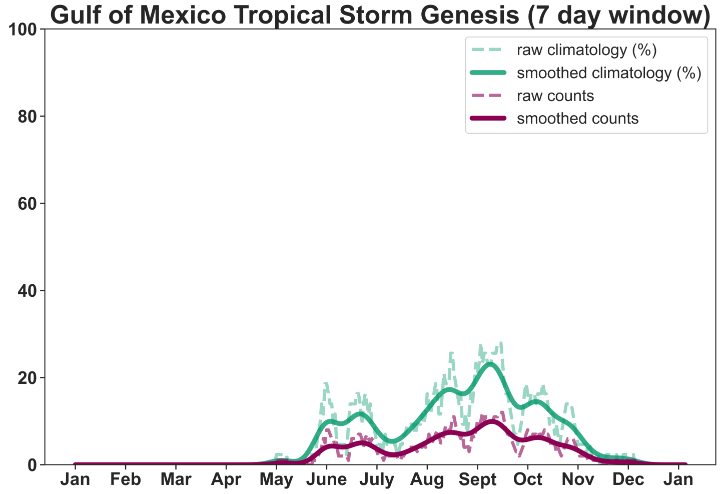

**Fig. A.1:** Hurricane climatology and hurricane counts for the Gulf of Mexico. The hurricane counts consists of all the storms that reached 34 knots added for each day of the year from 1979 to 2021. Solid lines are the smoothed climatology and counts, while the dashed lines are the corresponding raw data.

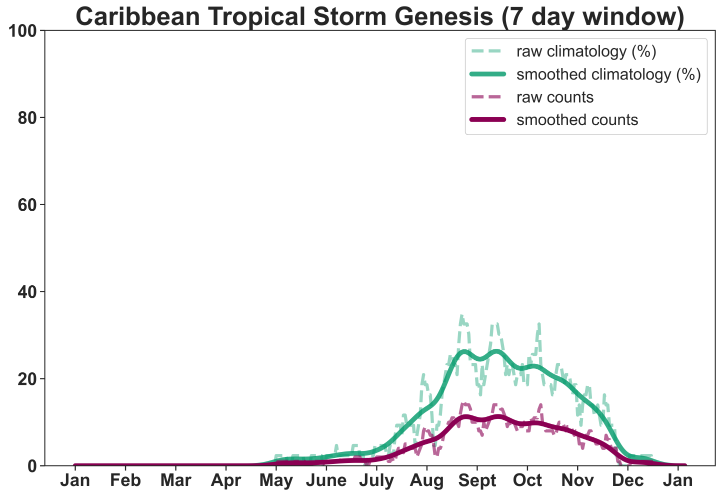

**Fig. A.2:** Hurricane climatology and hurricane counts for the Caribbean. The hurricane counts consists of all the storms that reached 34 knots added for each day of the year from 1979 to 2021. Solid lines are the smoothed climatology and counts, while the dashed lines are the corresponding raw data.

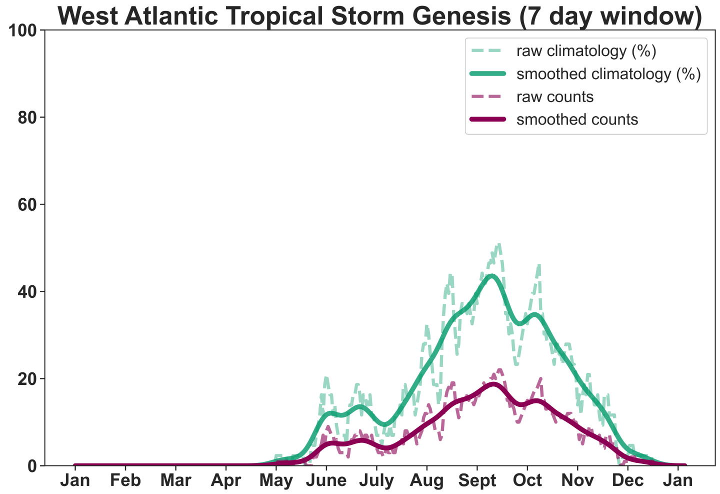

**Fig. A.3:** Hurricane climatology and hurricane counts for the West Atlantic. The hurricane counts consists of all the storms that reached 34 knots added for each day of the year from 1979 to 2021. Solid lines are the smoothed climatology and counts, while the dashed lines are the corresponding raw data.

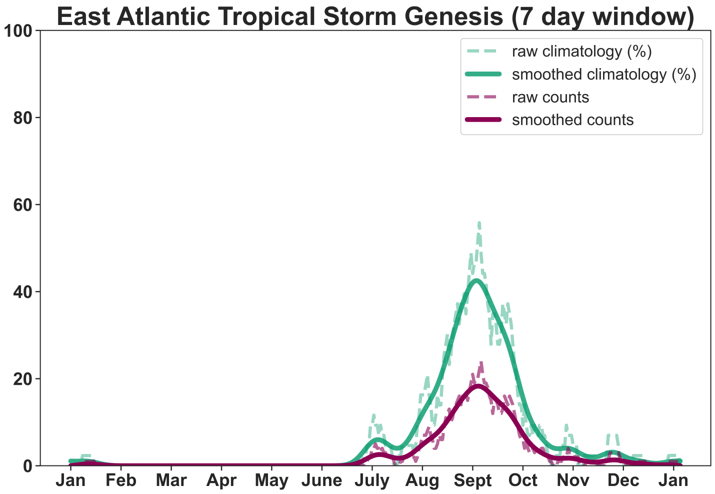

**Fig. A.4:** Hurricane climatology and hurricane counts for the East Atlantic. The hurricane counts consists of all the storms that reached 34 knots added for each day of the year from 1979 to 2021. Solid lines are the smoothed climatology and counts, while the dashed lines are the corresponding raw data.

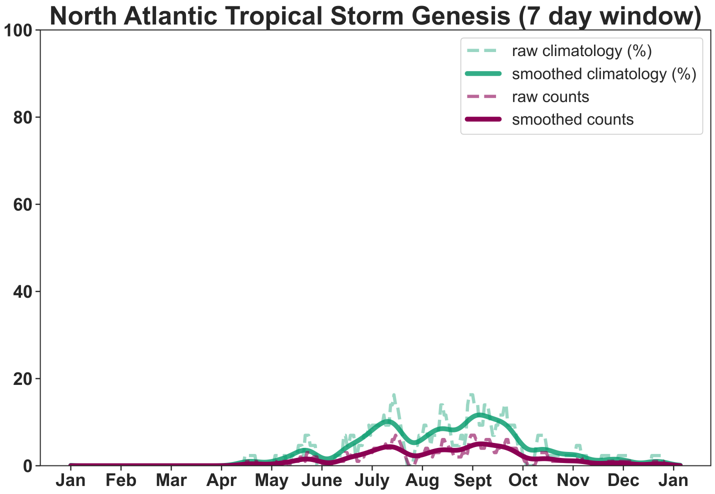

**Fig. A.5:** Hurricane climatology and hurricane counts for the North Atlantic. The hurricane counts consists of all the storms that reached 34 knots added for each day of the year from 1979 to 2021. Solid lines are the smoothed climatology and counts, while the dashed lines are the corresponding raw data.

# Appendix B

# LR and NN model comparisons for the Atlantic Subregions

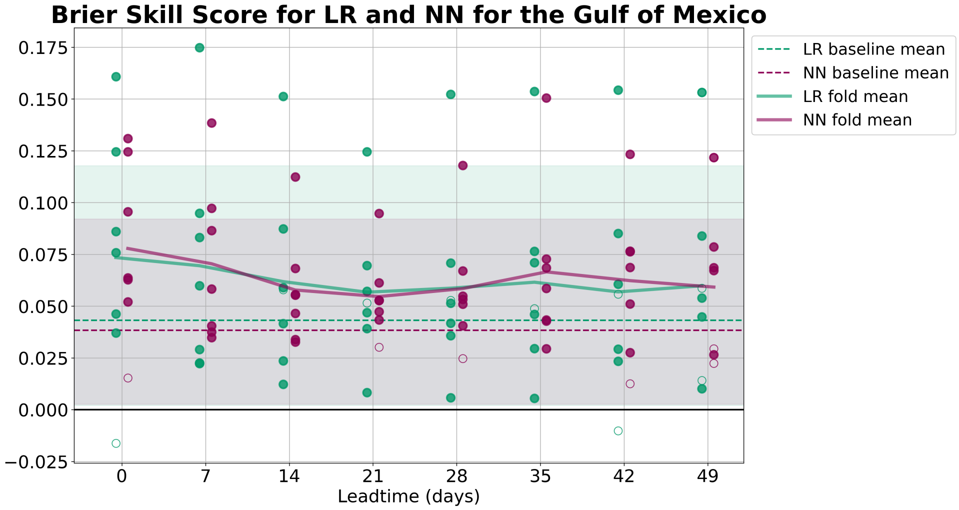

**Fig. B.1:** Comparing the brier skill score for the logistic regression and the neural network as a function of leadtime in the Gulf of Mexico. Closed circles indicate the folds that scored higher than the baseline, while the open circles indicate the folds with scores lower than the baseline. Input features are TC counts, ENSO, RMM1, RMM2, MDR SST, and AEW.

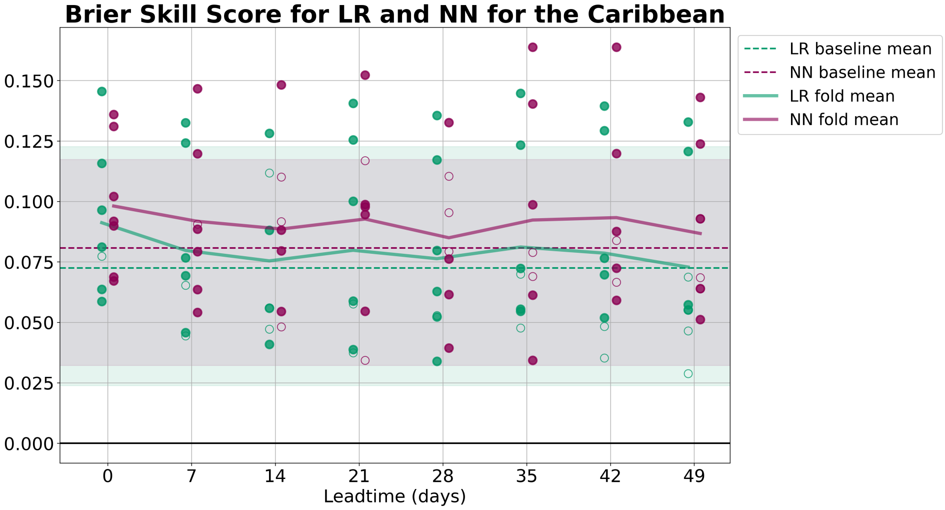

**Fig. B.2:** Comparing the brier skill score for the logistic regression and the neural network as a function of leadtime in the Caribbean. Closed circles indicate the folds that scored higher than the baseline, while the open circles indicate the folds with scores lower than the baseline. Input features are TC counts, ENSO, RMM1, RMM2, MDR SST, and AEW.

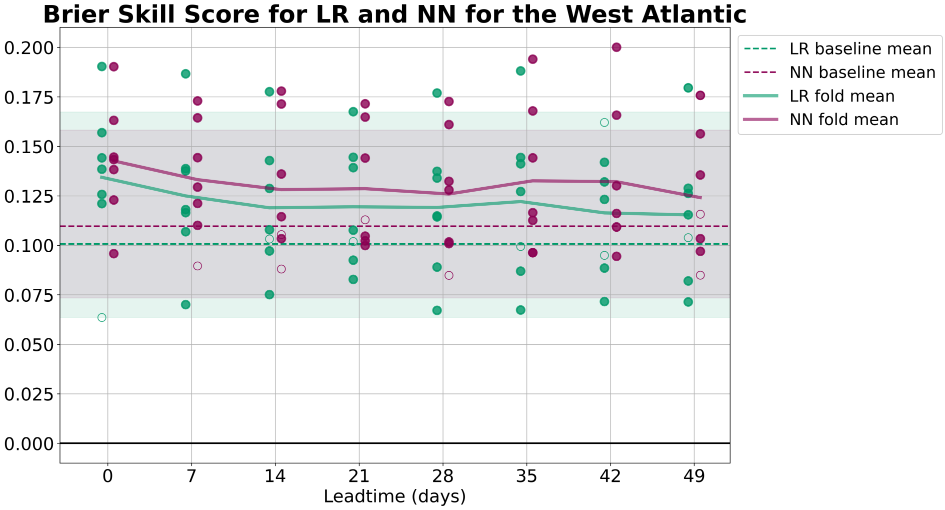

**Fig. B.3:** Comparing the brier skill score for the logistic regression and the neural network as a function of leadtime in the West Atlantic. Closed circles indicate the folds that scored higher than the baseline, while the open circles indicate the folds with scores lower than the baseline. Input features are TC counts, ENSO, RMM1, RMM2, MDR SST, and AEW.

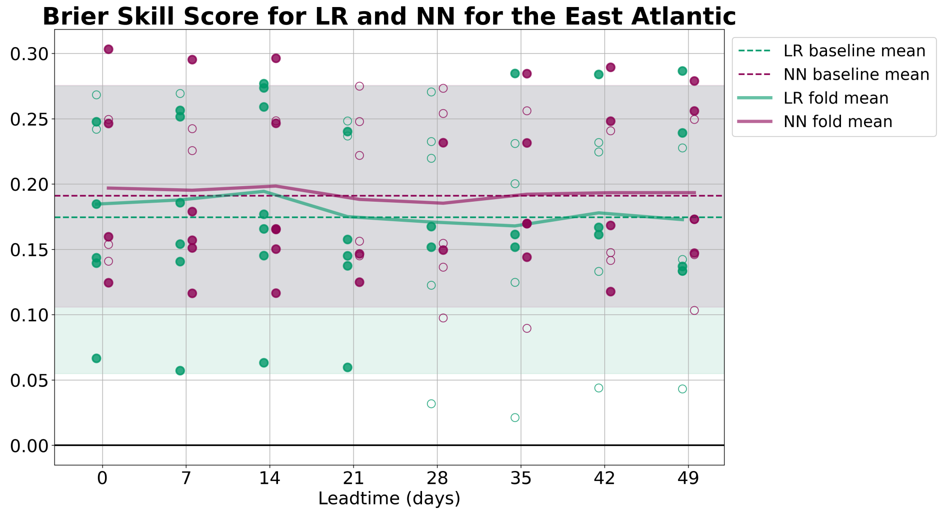

**Fig. B.4:** Comparing the brier skill score for the logistic regression and the neural network as a function of leadtime in the East Atlantic. Closed circles indicate the folds that scored higher than the baseline, while the open circles indicate the folds with scores lower than the baseline. Input features are TC counts, ENSO, RMM1, RMM2, MDR SST, and AEW.

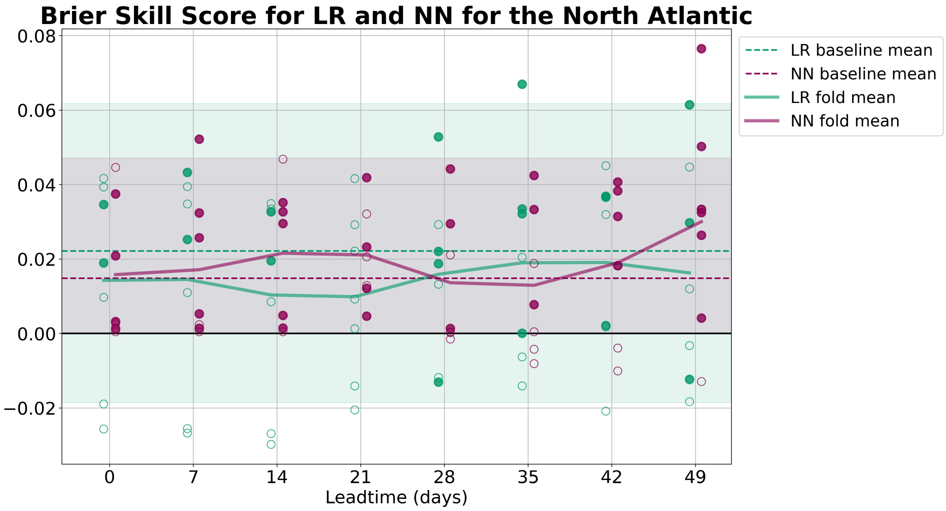

**Fig. B.5:** Comparing the brier skill score for the logistic regression and the neural network as a function of leadtime in the North Atlantic . Closed circles indicate the folds that scored higher than the baseline, while the open circles indicate the folds with scores lower than the baseline. Input features are TC counts, ENSO, RMM1, RMM2, MDR SST, and AEW.

# Appendix C

# NN model improvements over baseline for the Atlantic Subregions

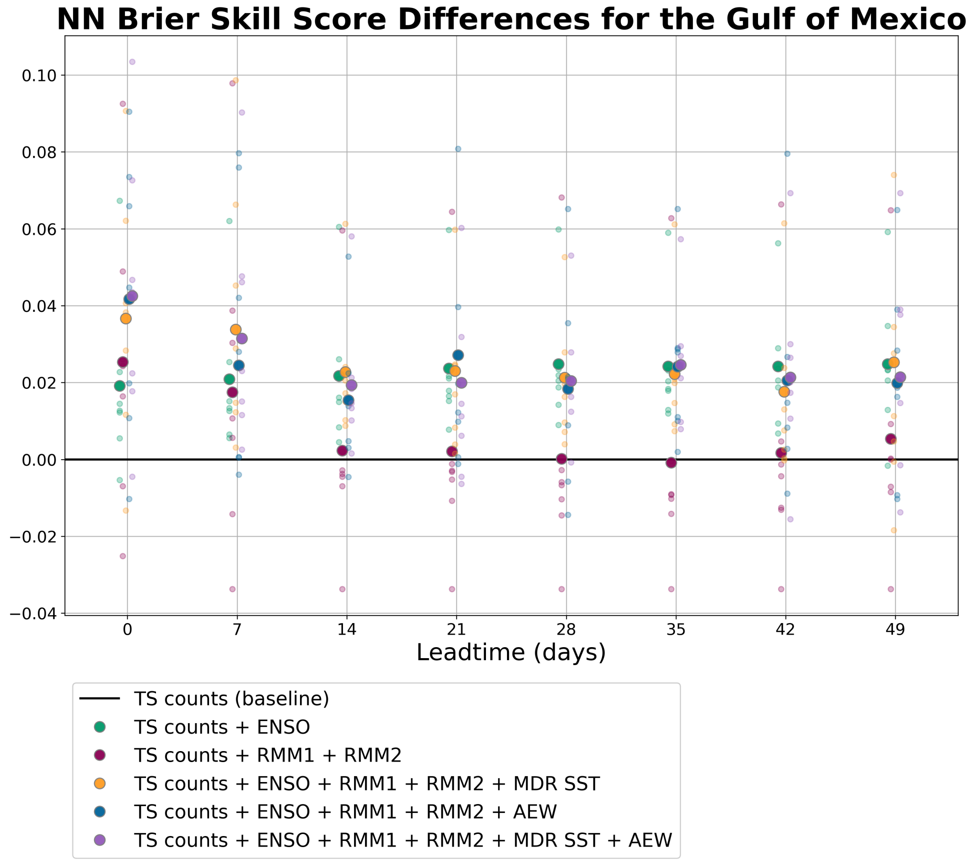

**Fig. C.1:** Brier skill scores and Brier skill score differences from the baseline for the NN models for the Gulf of Mexico using different feature combinations.

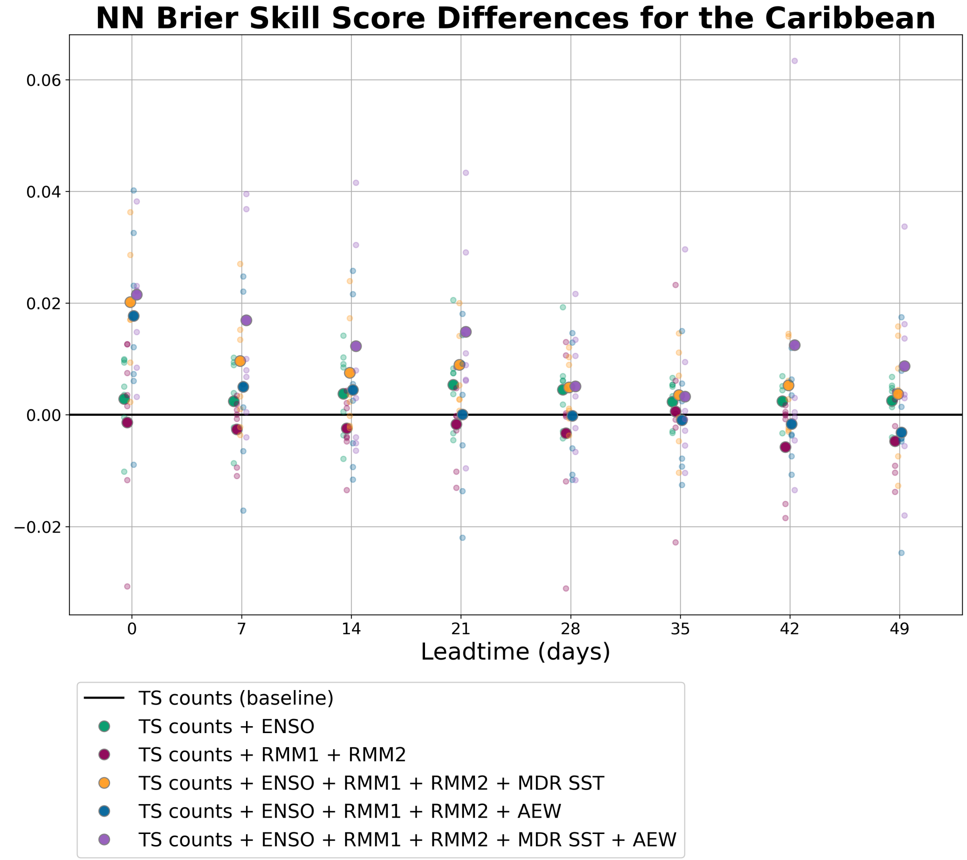

**Fig. C.2:** Brier skill scores and Brier skill score differences from the baseline for the NN models for the Caribbean using different feature combinations.

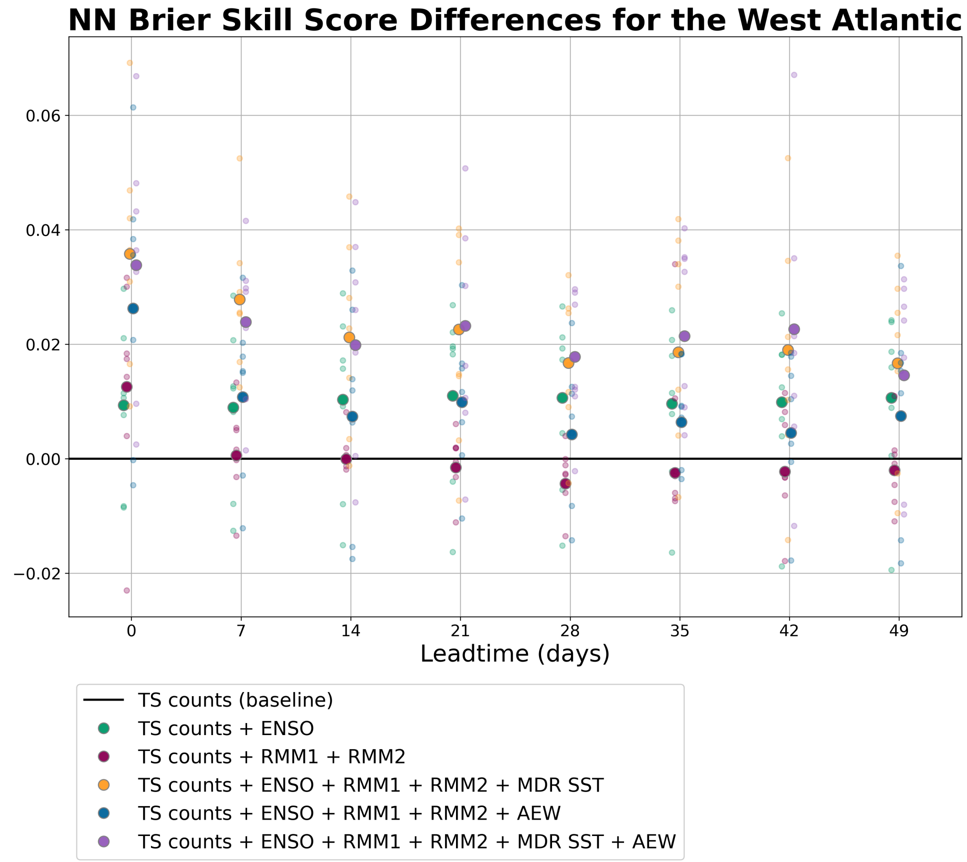

**Fig. C.3:** Brier skill scores and Brier skill score differences from the baseline for the NN models for the west Atlantic using different feature combinations.

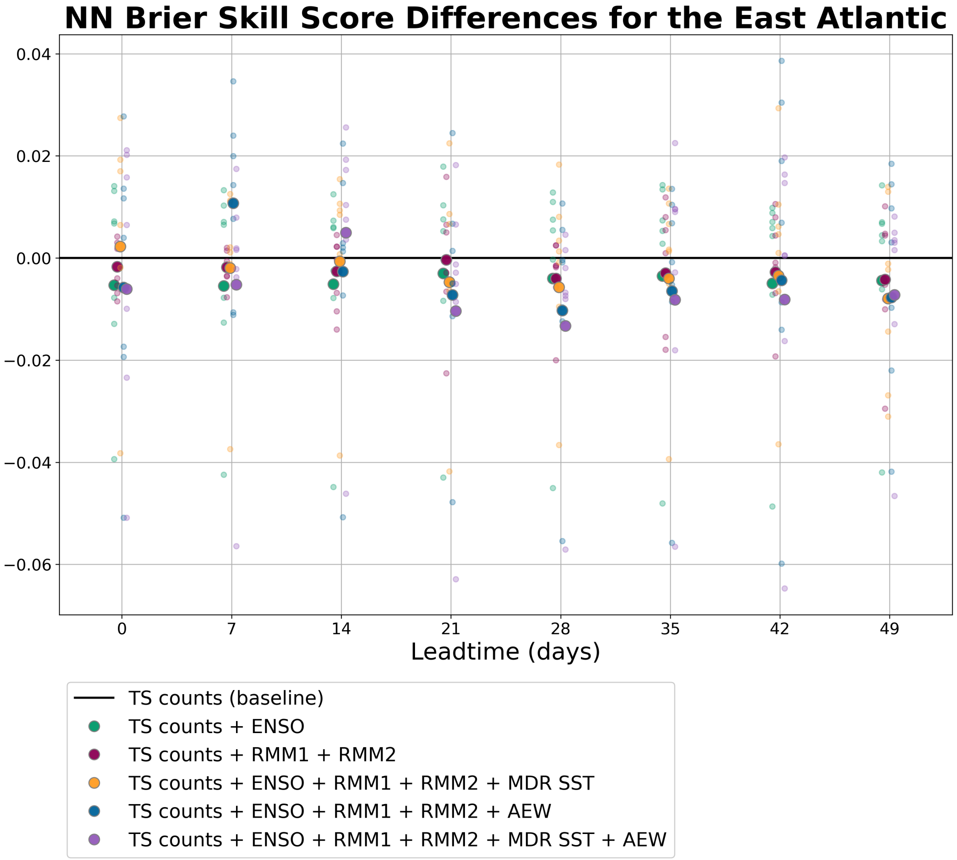

**Fig. C.4:** Brier skill scores and Brier skill score differences from the baseline for the NN models for the east Atlantic using different feature combinations.

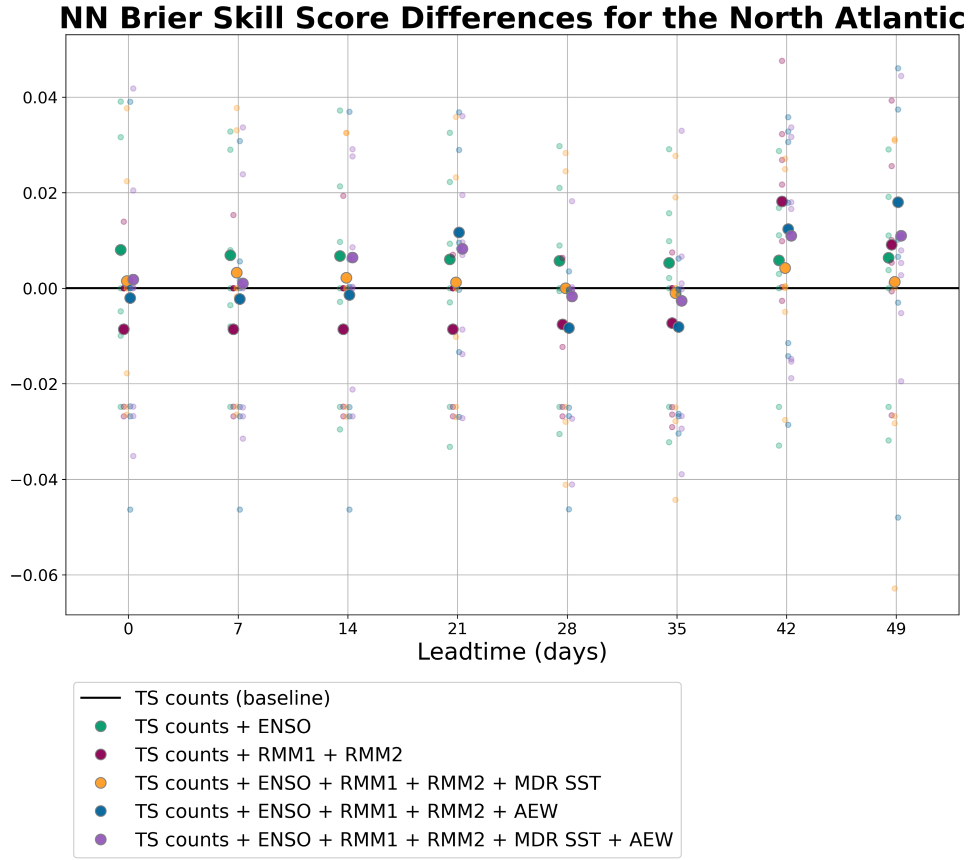

**Fig. C.5:** Brier skill scores and Brier skill score differences from the baseline for the NN models for the north Atlantic using different feature combinations.

# Appendix D

# AEW index timeseries

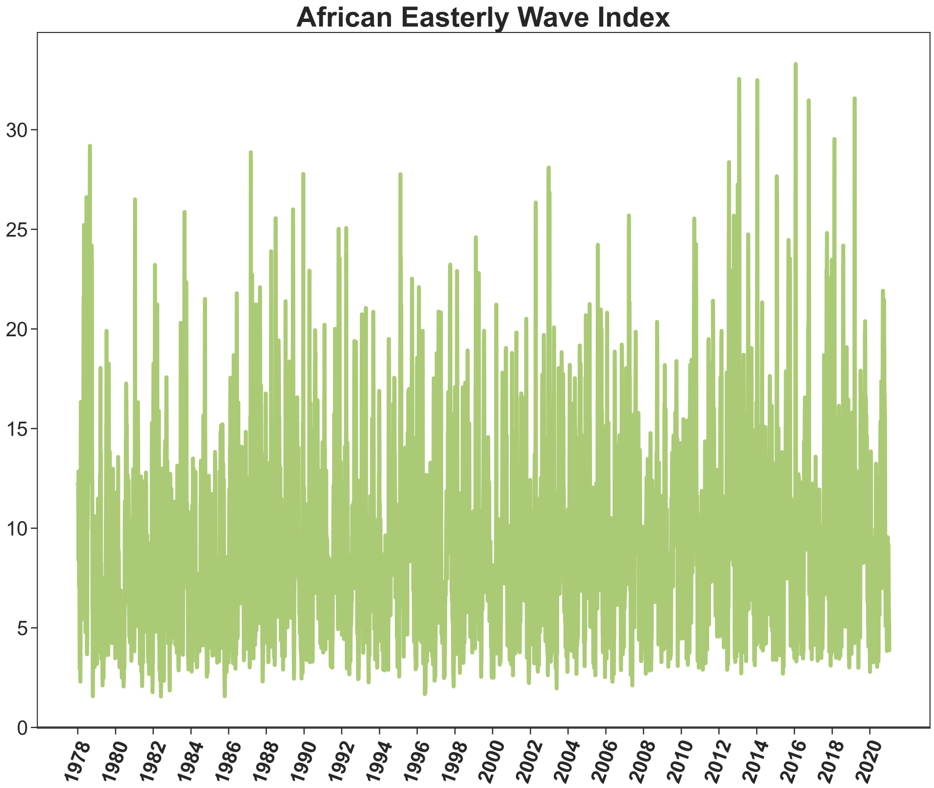

**Fig. D.1:** AEW index timeseries

# Appendix E

# MJO, ENSO, SST, U850, AEW, and MDR SSTs for 1983 and 2021

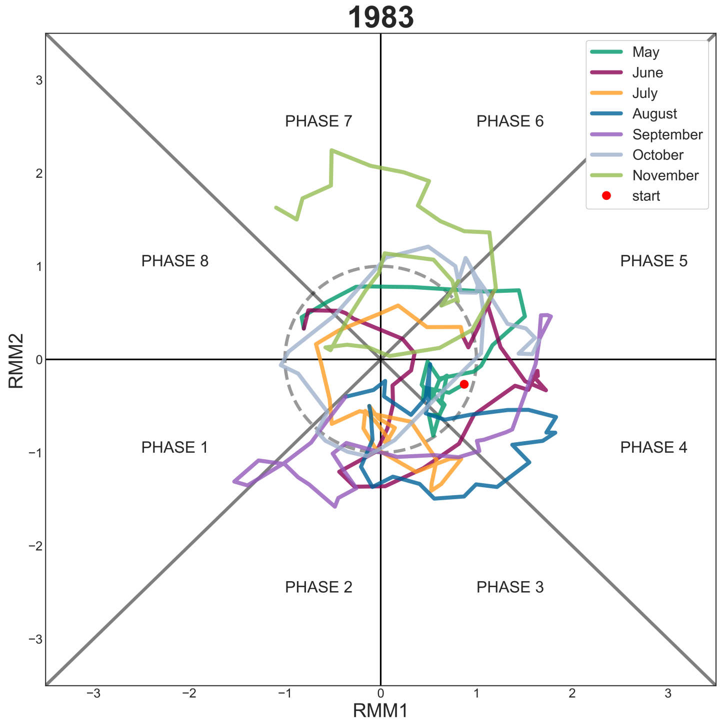

**Fig. E.1:** RMM1 and RMM2 in phase space throughout the year 1983.

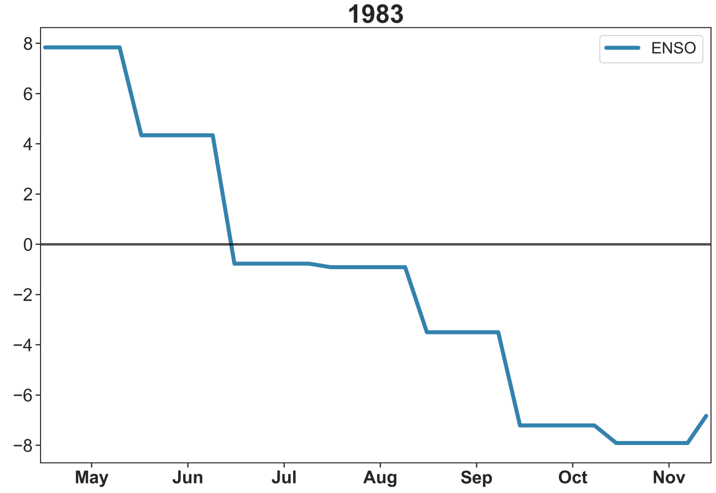

**Fig. E.2:** ENSO values throughout the year 1983.

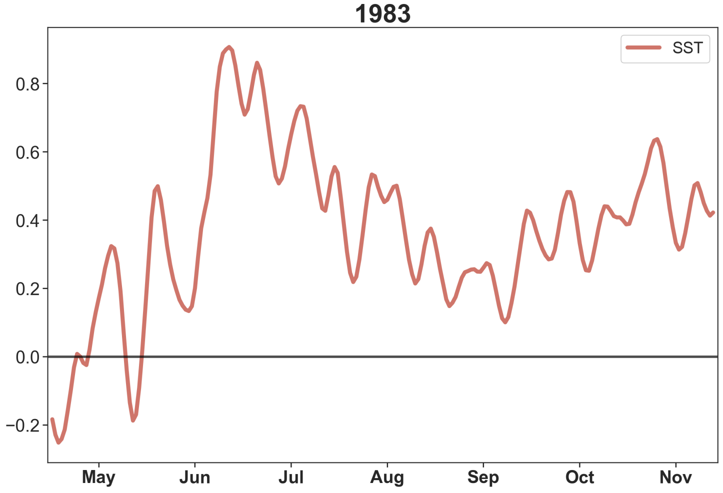

**Fig. E.3:** SST values between $5° - 18°$ N, $90° - 115°$ W throughout the year 1983.

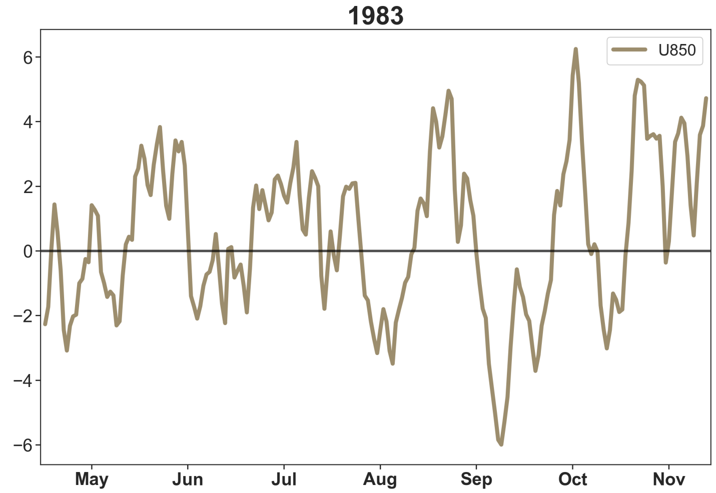

**Fig. E.4:** 850 mb zonal winds within 5° − 15° N, 85° − 125° W throughout the year 1983.

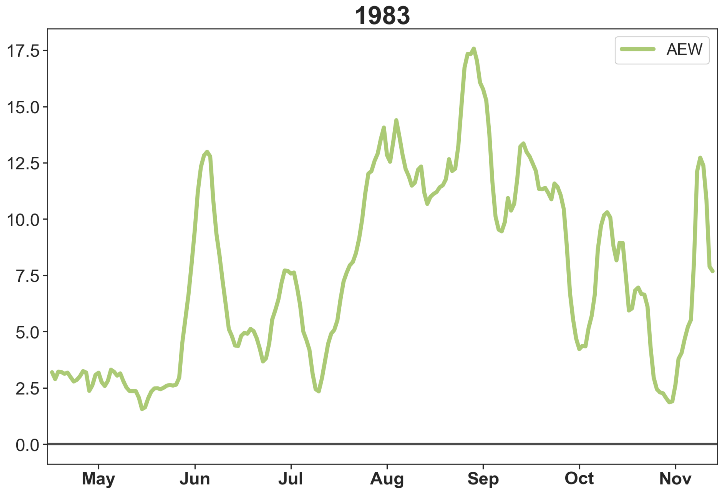

**Fig. E.5:** AEW index throughout the year 1983.

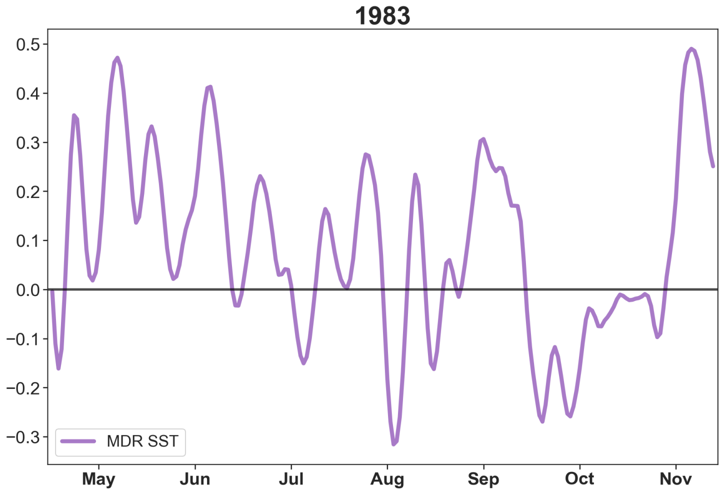

**Fig. E.6:** MDR (5° − 18° N, 20° − 60° W) SST values throughout the year 1983. Positive anomalies represent westerly winds, while negative represent easterly.

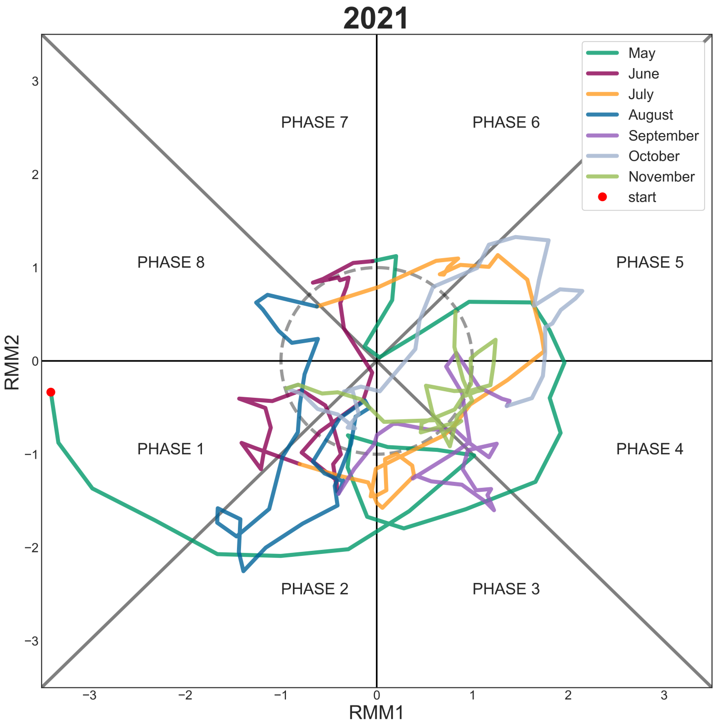

**Fig. E.7:** RMM1 and RMM2 in phase space throughout the year 2021.

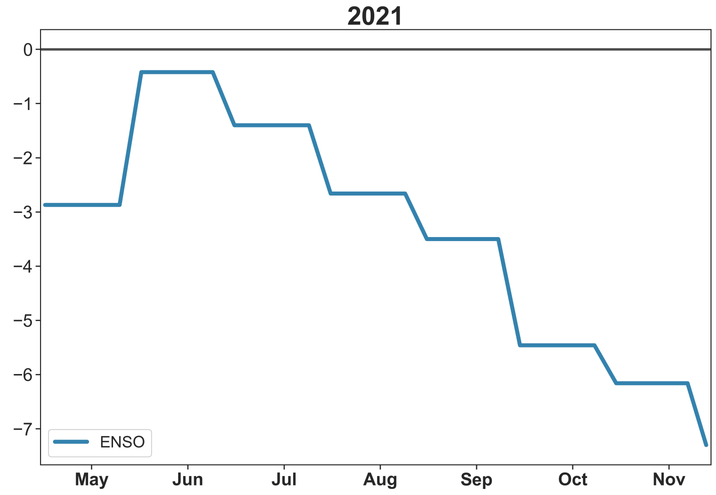

**Fig. E.8:** ENSO values throughout the year 2021.

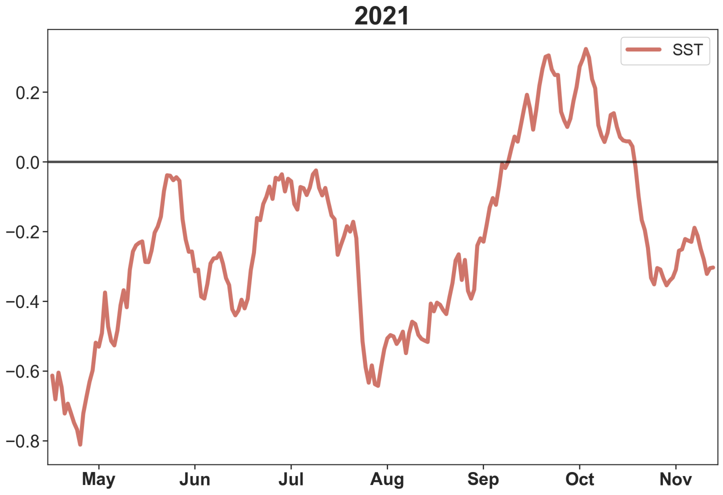

**Fig. E.9:** SST values between $5° - 18°$ N, $90° - 115°$ W throughout the year 2021.

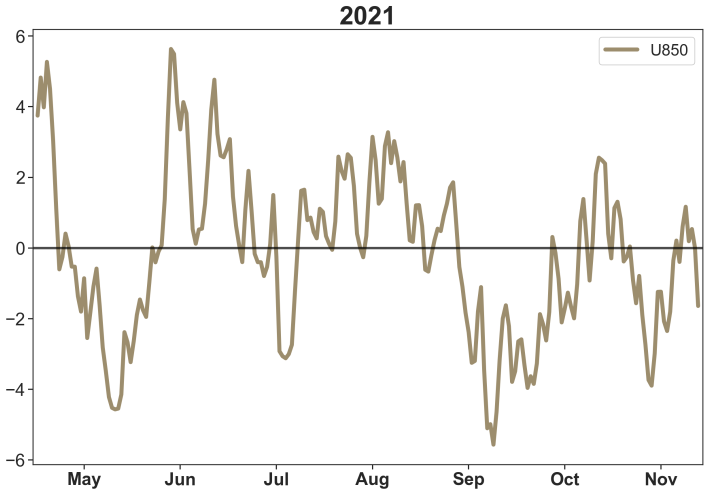

**Fig. E.10:** 850 mb zonal winds within 5° − 15° N, 85° − 125° W throughout the year 2021. Positive anomalies represent westerly winds, while negative represent easterly.

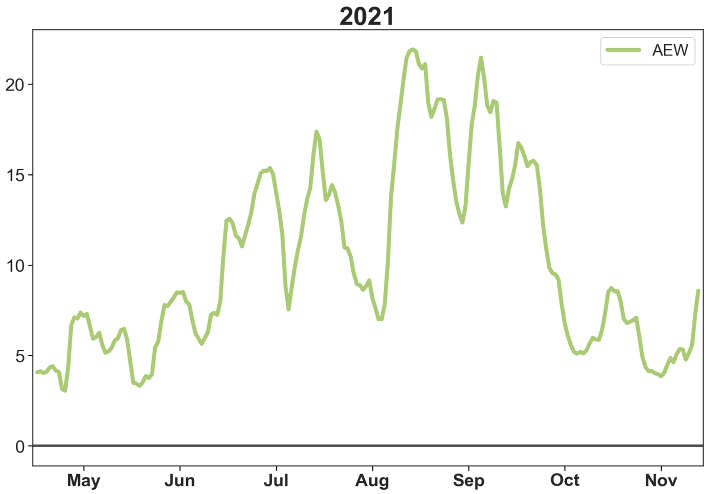

**Fig. E.11:** AEW index throughout the year 2021.

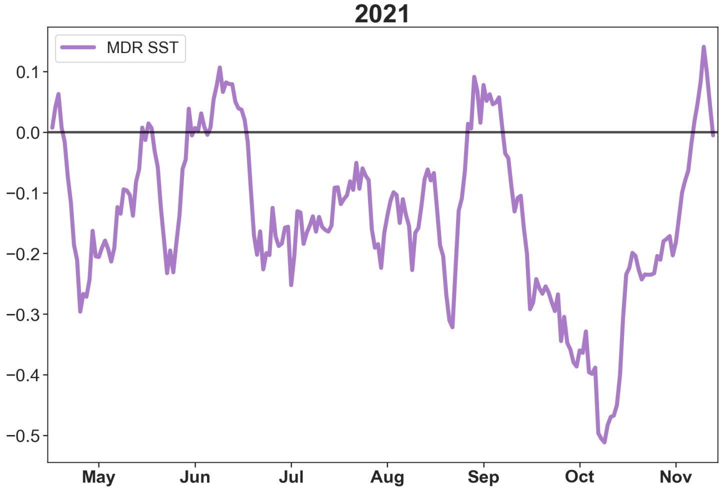

**Fig. E.12:** MDR ($5^\circ - 18^\circ$ N, $20^\circ - 60^\circ$ W) SST values throughout the year 2021.

# Appendix F

# NN 2021 predictions and SHAP values in the Atlantic Subregions

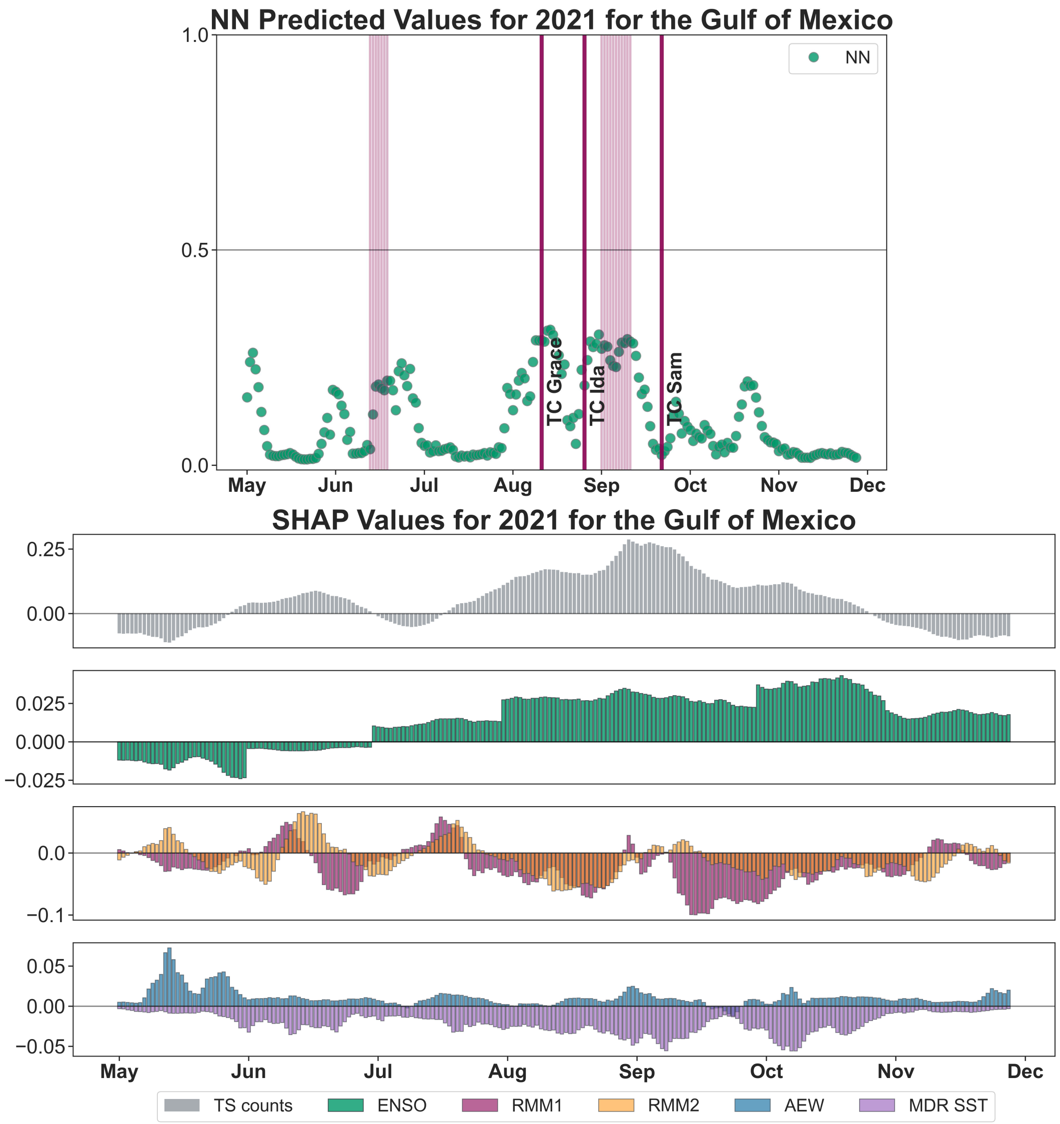

**Fig. F.1:** Probabilities and SHAP values. (a) The circles indicate the predicted TC days, and the shaded lines are the days where TC were observed in the Gulf of Mexico in 2021. (b) The variable importances according to the NN. Features with positive SHAP values pushed the model towards forecasting TCs that day, while variables with negative SHAP values pushed the model towards a forecast of no TCs.

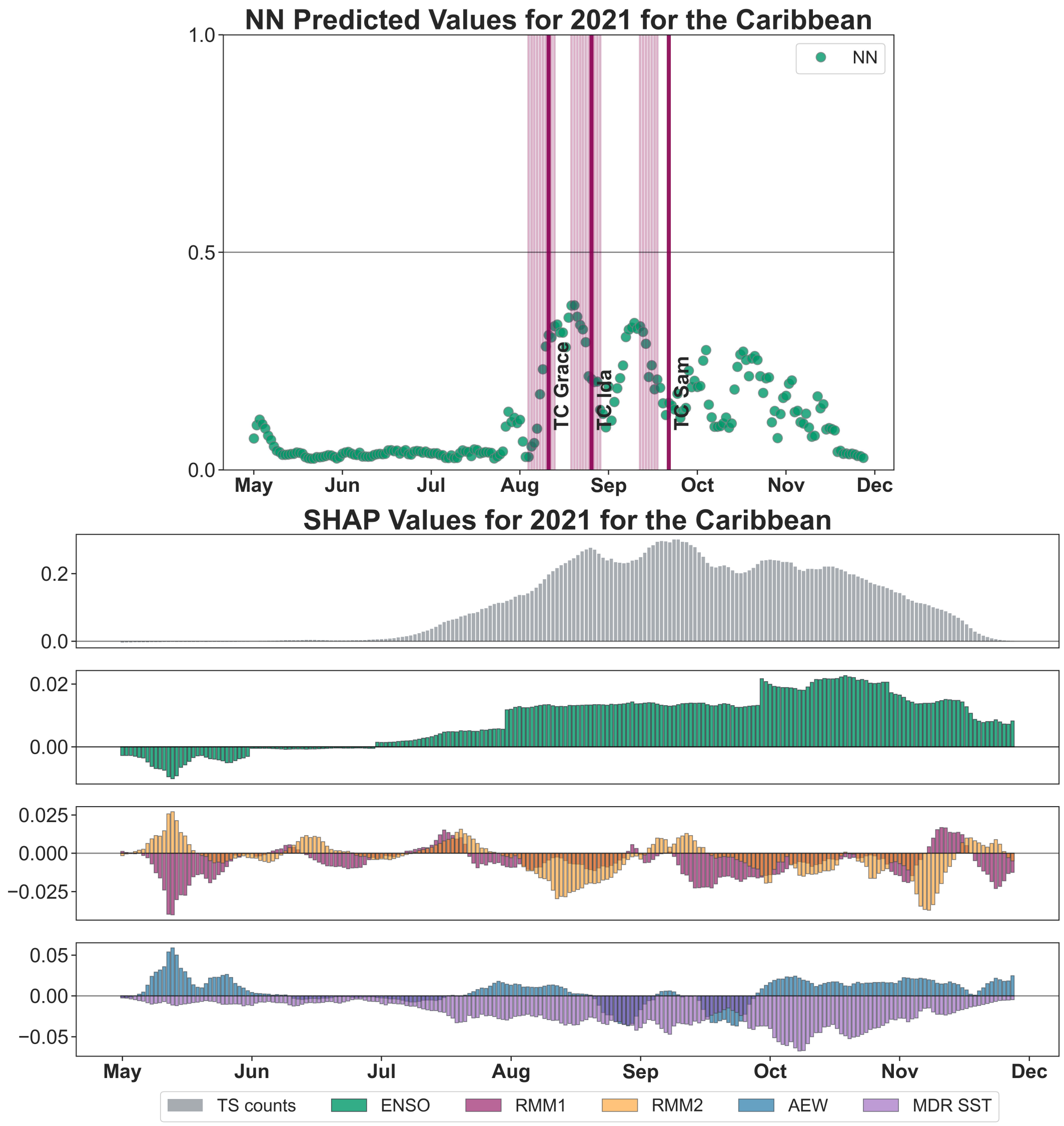

**Fig. F.2:** Probabilities and SHAP values. (a) The circles indicate the predicted TC days, and the shaded lines are the days where TC were observed in the Caribbean in 2021. (b) The variable importances according to the NN. Features with positive SHAP values pushed the model towards forecasting TCs that day, while variables with negative SHAP values pushed the model towards a forecast of no TCs.

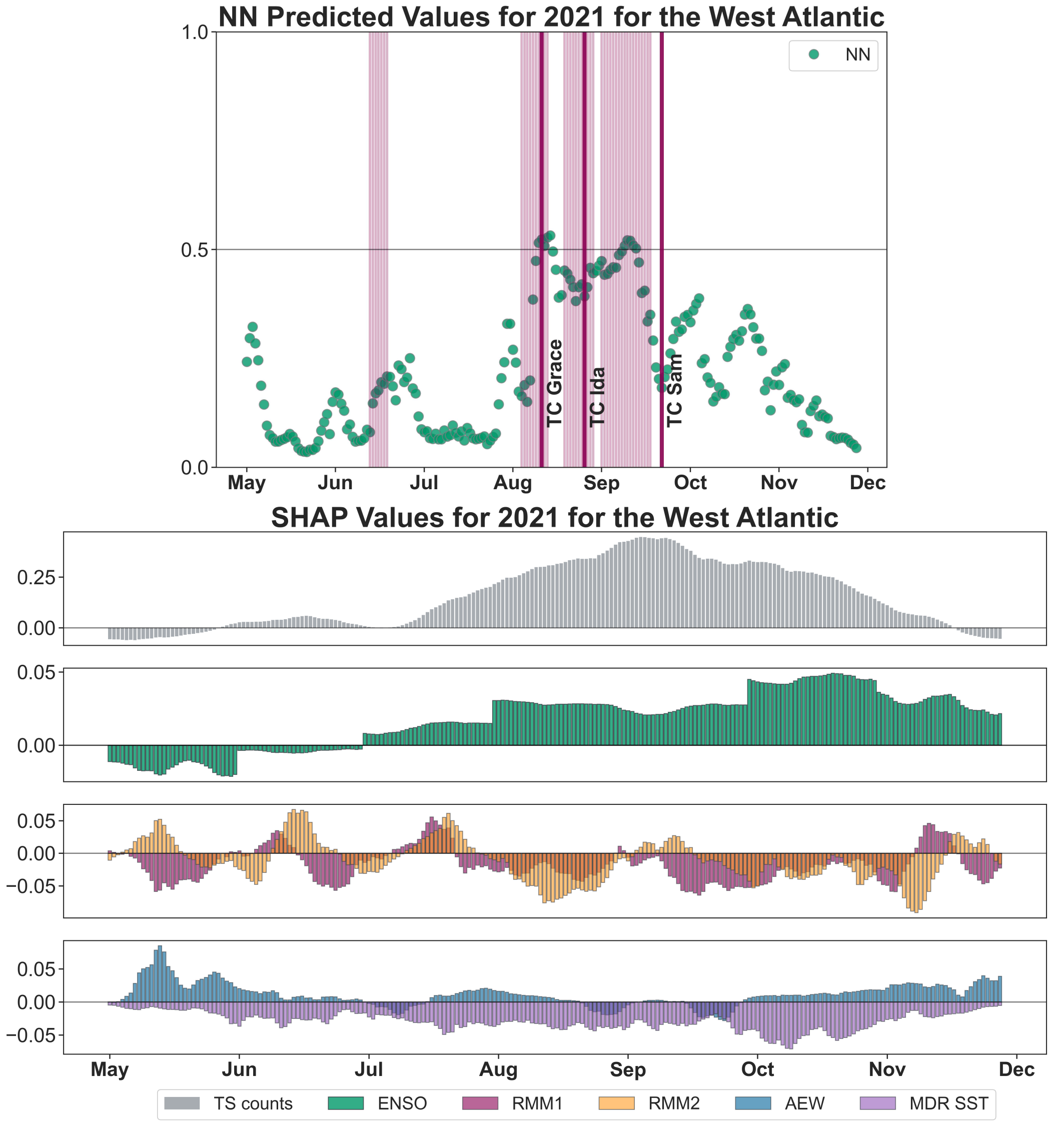

**Fig. F.3:** Probabilities and SHAP values. (a) The circles indicate the predicted TCs days, and the shaded lines are the days where TCs were observed in the West Atlantic in 2021. (b) The variable importances according to the NN. Features with positive SHAP values pushed the model towards forecasting TCs that day, while variables with negative SHAP values pushed the model towards a forecast of no TCs.

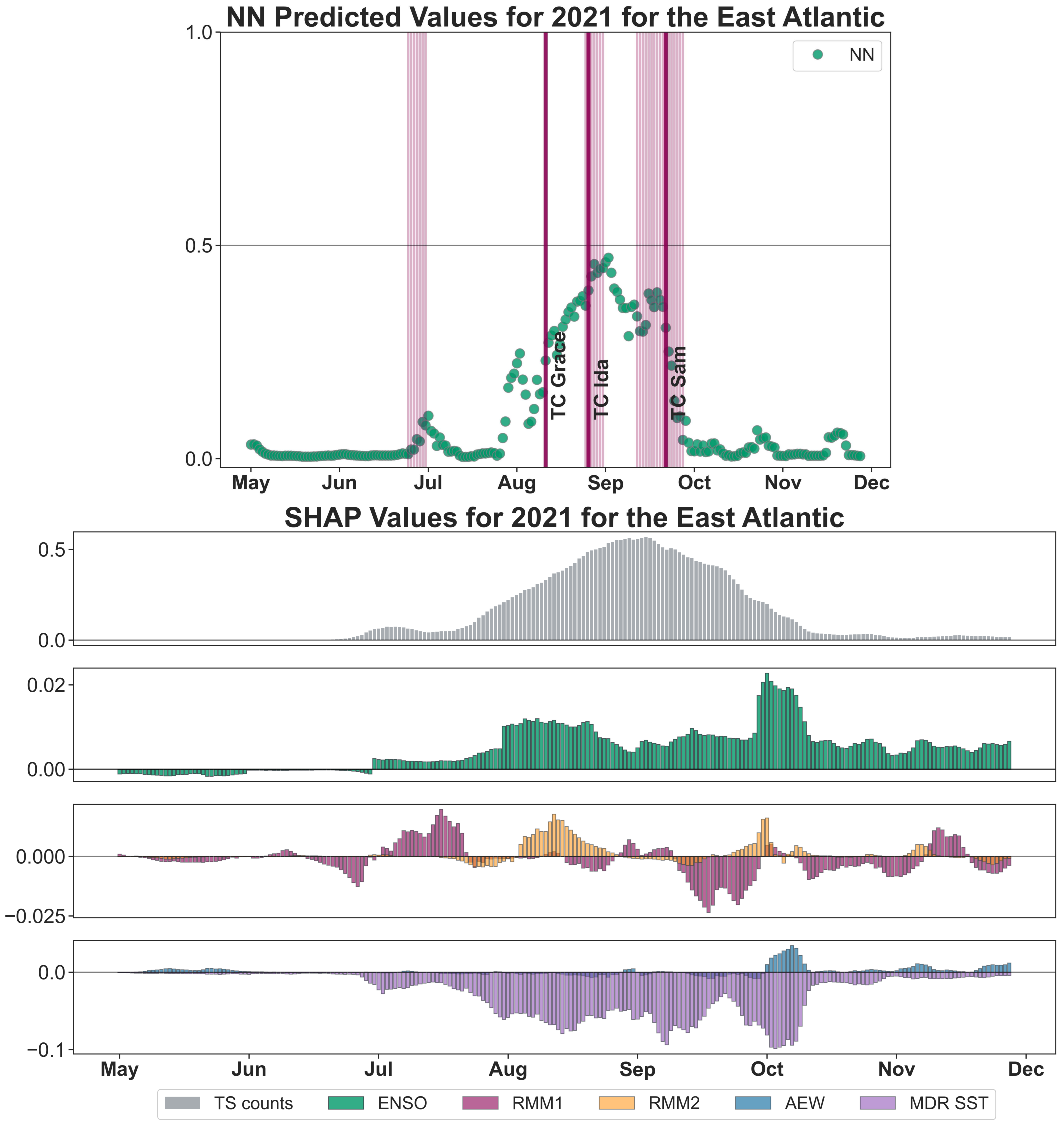

**Fig. F.4:** Probabilities and SHAP values. (a) The circles indicate the predicted TC days, and the shaded lines are the days where TCs were observed in the East Atlantic in 2021. (b) The variable importances according to the NN. Features with positive SHAP values pushed the model towards forecasting TCs that day, while variables with negative SHAP values pushed the model towards a forecast of no TC.

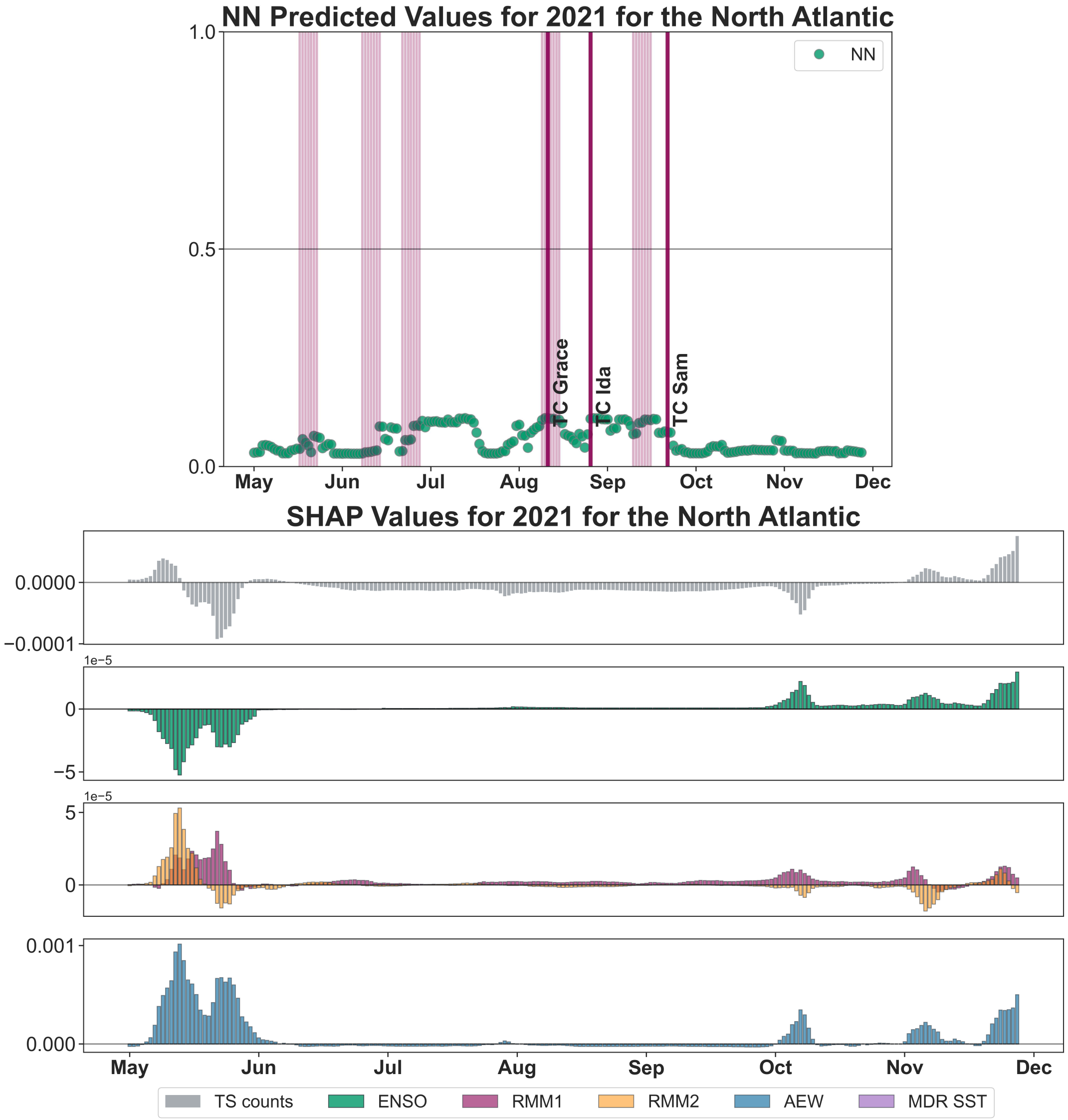

**Fig. F.5:** Probabilities and SHAP values. (a) The circles indicate the predicted TC days, and the shaded lines are the days where TCs were observed in the North Atlantic in 2021. (b) The variable importances according to the NN. Features with positive SHAP values pushed the model towards forecasting TCs that day, while variables with negative SHAP values pushed the model towards a forecast of no TCs.

# Appendix G

# Loss values for different NN architectures

**Table G.1:** East Pacific Loss Values at 30 Epochs for Several Architectures

| **nodes** | **single layer loss [x]** | **double layer loss [x,x]** |
|---|---|---|
| 1 | 0.662 | 0.575 |
| 2 | 0.572 | 0.573 |
| 3 | 0.574 | 0.573 |
| 4 | 0.571 | 0.572 |
| 5 | 0.571 | 0.572 |
| 6 | 0.571 | 0.571 |
| 7 | 0.571 | 0.571 |
| 10 | 0.571 | 0.571 |
| 15 | 0.571 | 0.571 |
| 20 | 0.571 | 0.571 |
| 25 | 0.571 | 0.571 |
| 50 | 0.571 | 0.570 |
| 75 | 0.571 | 0.570 |
| 100 | 0.570 | 0.570 |

**Table G.2:** Atlantic Loss Values at 30 Epochs for Several Architectures

| **nodes** | **single layer loss [x]** | **double layer loss [x,x]** |
|---|---|---|
| 1 | 0.622 | 0.622 |
| 2 | 0.526 | 0.525 |
| 3 | 0.622 | 0.622 |
| 4 | 0.622 | 0.622 |
| 5 | 0.524 | 0.617 |
| 6 | 0.523 | 0.524 |
| 7 | 0.524 | 0.524 |
| 10 | 0.524 | 0.523 |
| 15 | 0.523 | 0.523 |
| 20 | 0.523 | 0.523 |
| 25 | 0.523 | 0.523 |
| 50 | 0.523 | 0.522 |
| 75 | 0.523 | 0.522 |
| 100 | 0.522 | 0.522 |